

Phase-field cohesive zone modeling of multi-physical fracture in solids and the open-source implementation in COMSOL MULTIPHYSICS

Wan-Xin Chen^a, Jian-Ying Wu^{a,b,*}

^a Department of Civil Engineering, South China University of Technology, 510641 Guangzhou, China

^b State Key Laboratory of Subtropical Building Science, South China University of Technology, 510641 Guangzhou, China

ARTICLE INFO

Keywords:

Phase-field
Multi-physics
Fracture
Hydrogen assisted cracking
Thermal shock
Piezoelectric solids

ABSTRACT

Despite the popularity of phase-field models for fracture in purely mechanical problems, their application to the modeling of fracture in multi-physics problems is much less reported. This might be attributed, on the one hand, to the theoretical complexity involved in multi-physical phenomena, and on the other hand, to the cumbersome implementation of these coupled models in home-made platforms. In this work, the phase-field cohesive zone model (PF-CZM) is adopted as the prototype model to address fracture in various multi-physics problems, e.g., the thermo-mechanical, chemo-mechanical, chemo-thermo-mechanical, electro-mechanical, etc. The relevant theoretical and numerical aspects are categorized into modular structures, and the open-source implementations in the software platform COMSOL MULTIPHYSICS are presented in details. In order to validate the PF-CZM for fracture in multi-physics problems and its numerical implementation, a number of representative benchmark examples are considered. Not only the qualitative crack patterns but also the quantitative global responses are compared against available experimental test data. It is found that the typical characteristics of fracture in all the considered multi-physics problems are well captured. Moreover, as in the purely mechanical counterpart, the predicted crack pattern and global responses are insensitive to the phase-field length scale, making the PF-CZM promising for modeling fracture in other more involved multi-physics problems.

1. Introduction

During the service lifecycle, engineering structures are threatened by extreme mechanical loading and also deteriorated by harsh environmental actions involving thermal, hydraulic, chemical and electric effects. In such multi-physical scenarios, cracking-induced fracture might be the most commonly encountered failure mode in solids and structures. Therefore, it is of vital significance to predict nucleation and propagation of the crack in solids and quantify their adverse effects on the integrity of structures. For those multi-physics problems involving spatial and temporal scales where experimental tests are difficult or impossible to perform, the computer simulation is a feasible approach and sometimes the only one that provides tremendous useful information for studying cracking-induced localized failure in solids and structures.

In last a few decades, various emerging approaches have been proposed to study cracks evolution and predict the resulting failure in solids [1]. Here we are limited ourselves to the phase-field damage model for fracture set forth by Francfort and Marigo [2] and Bourdin et al. [3]. Ever since the work of Miehe et al. [4], this approach has attracted a lot of attention in the computational mechanics community

and develops as one of the most promising candidates in the computational failure mechanics. The popularity is attributed largely to their intrinsic capability in dealing with 2-D and 3-D complex crack configurations involving arbitrary nucleation, propagation, branching, merging, coalesces and fragmentation in a single standalone framework [5], with no need of any *ad hoc* fracture criterion or extrinsic crack tracking algorithm; see [6,7] for the extensive reviews.

In phase-field models for fracture, the sharp crack is regularized by a diffuse crack band measured by the so-called phase-field length scale. Moreover, an extra field variable, i.e., the crack phase-field or damage field continuously distributed in the solid, is introduced to represent the crack configuration, with zero being the intact bulk, one being the sharp crack and the in-between value representing a specific intermediate state, respectively. Even though they can be extended to ductile fracture with plasticity theory incorporated [6,8,9], earlier phase-field models, e.g., the AT2 [3,10], AT1 [11] and other variants [12], apply predominantly to brittle fracture, since they converge in the context of Γ -convergence to Griffith's theory [13] for brittle fracture. Moreover, the predicted global responses are sensitive to the phase-field length scale — when it is smaller, the peak load is higher, and the failure

* Corresponding author at: State Key Laboratory of Subtropical Building Science, South China University of Technology, 510641 Guangzhou, China.
E-mail address: jywu@scut.edu.cn (J.-Y. Wu).

strength becomes infinite for a vanishing length scale. Consequently, crack nucleation cannot be dealt with if the phase-field length scale is treated as a numerical parameter. To address this issue, it is now a common consensus that in such models the phase-field length scale should be treated as a physical property related to Irwin's characteristic length [14,15]. At the cost of losing the favored Γ -convergence, this new interpretation of the phase-field length scale works for most brittle fracture [15] but some exceptions still exist [16,17]. Moreover, quasi-brittle failure with general softening curves cannot be considered — the phase-field length scale so-determined is usually too large to reproduce the correct crack pattern and accurate global responses simultaneously [14,18].

Recently, Wu [19–21] established a unified phase-field theory for damage and fracture in solids, incorporating the classical AT1 and AT2 phase-field models for brittle fracture as its particular instances. Moreover, with the failure strength introduced as an independent material property, a phase-field cohesive zone model, or in short, PF-CZM, which applies to both brittle fracture and quasi-brittle failure, was proposed. The PF-CZM converges upon a vanishing phase-field length scale to the Barenblatt cohesive zone model (CZM) [22], and various traction-separation laws (TSL) can be reproduced or approximated with high precision. Importantly, it incorporates seamlessly *the strength-based crack nucleation criterion and the energy-based crack propagation criterion*, possessing some unique merits over those phase-field models for brittle fracture. For instance, crack nucleation can be considered with no *ad hoc* modification, and the predicted global responses are sensitive neither to the mesh size/alignment nor to the phase-field length scale. Accordingly, the PF-CZM has been applied successfully to fracture in purely mechanical problems, etc., static fracture [23,24], dynamic fracture [25,26], fatigue fracture [27,28], etc.

As mentioned before, multi-physical processes due to harsh environmental effects generally promote fracture in solids. Fortunately, even the phase-field model for purely mechanical fracture is intrinsically a multi-field coupling approach — the governing equations consist of the standard macroscopic equilibrium ones for the displacement field and the microscopic evolution laws for the crack phase-field. Therefore, it is readily extended to fracture in more complex multi-physics problems, e.g., thermal effects induced cracking in solids [29,30], electromechanical fracture of piezoelectric solids [31–33], chemo-thermo-mechanical (shrinkage induced) cracking in early-age concrete [34,35], hydrogen-assisted cracking in metals [36,37], diffusion of chloride ions induced cracking in cement paste [38], calcite dissolution induced fracture in concrete exposed to CO₂ [39], among many others. However, except very few examples [40–42], most multi-physical extensions employ the AT1 and AT2 models for brittle fracture as the prototype model. Consequently, the aforesaid issues present again — neither crack nucleation in brittle fracture nor quasi-brittle failure can be dealt with satisfactorily. Moreover, the inter-field couplings between different physical processes are complicated and can occur at the distinct levels of governing equations and/or constitutive relations. A systematical study on the phase-field modeling of fracture in multi-physics problems is lacking.

Besides the above theoretical aspects, another non-negligible challenging issue in the phase-field modeling of fracture in multi-physics problems is the numerical implementation. In the literature, either home-made platforms, e.g. MEF90 [5], FENICS [43,44], DEAL.II [45–47], MOOSE [48,49], MATLAB [50,51], JIVE [52], etc., or commercial software packages, e.g., ABAQUS [53–57], LS-DYNA [58] and COMSOL MULTIPHYSICS [59–61], have been adopted. Among them, most are limited to purely mechanical cases largely because of the cumbersome implementation for the much more involved multi-physical problems. Even for the all-in-one and general purpose oriented platform COMSOL MULTIPHYSICS, its potential to multi-physical problems is far from being explored in the phase-field community. For instance, the strategy dealing with the crack irreversibility condition suggested in [60] is inconsistent and might lead to imprecise or even erroneous results. And the indirect

displacement control, which is very useful to deal with localized failure involving snap-backs, has yet been perused in this platform.

Aiming to address the above issues, this work addresses systematically the phase-field cohesive zone modeling of fracture in multi-physics problems and the open-source implementation in COMSOL MULTIPHYSICS. More specifically, the phase-field cohesive zone model (PF-CZM) is adopted as the prototype model to address fracture in various classical multi-physics problems, e.g., the thermo-mechanical, chemo-mechanical, chemo-thermo-mechanical and electromechanical ones, etc. The involved theoretical and numerical aspects are categorized into modular structures, and the open-source implementations are presented in COMSOL MULTIPHYSICS. This platform is selected since the governing equations in strong form can be directly implemented and then automatically solved with the multi-field finite element method in a staggered or monolithic scheme. In order to validate the PF-CZM for fracture in multi-physics problems and the numerical implementation, a number of representative benchmark examples are considered. The crack patterns and global responses are compared qualitatively and quantitatively against available experimental test data. Note that the theoretical and numerical aspects presented in this work are rather general and can be easily adapted to other more involved multi-physics problems like hydraulic fracture.

The remainder of this paper is organized as follows. The theoretic aspects of the PF-CZM for fracture in various multi-physics problems are addressed in Section 2 in modular structures of governing equations and constitutive relations. Subsequently, the numerical aspects concerning implementations of these phase-field models in COMSOL MULTIPHYSICS are reported at length in Section 3. Representative benchmark examples under purely mechanical and multi-physical scenarios involving both brittle fracture and quasi-brittle failure are presented in Section 4. The relevant conclusions are drawn in Section 5.

Notation. Compact tensor notation is used in the theoretical part of this paper. As general rules, scalars are denoted by italic light-face Greek or Latin letters (e.g. a or λ); vectors, second- and fourth-order tensors are signified by italic boldface minuscule, majuscule and blackboard-bold majuscule characters like \mathbf{a} , \mathbf{A} and \mathbb{A} , respectively. For instance, $\mathbf{1}$ and \mathbb{I} represent the second- and symmetric fourth-order identity tensors, respectively. The inner products with single and double contractions are denoted by \cdot and $\cdot\cdot$, respectively. The dyadic products \otimes and $\overline{\otimes}$ are defined as

$$\mathbf{a} \otimes \mathbf{B} = a_i B_{jk} \mathbf{e}_i \mathbf{e}_j \mathbf{e}_k \quad \mathbf{a} \overline{\otimes} \mathbf{B} = \frac{1}{2} (a_j B_{ik} + a_k B_{ij}) \mathbf{e}_i \mathbf{e}_j \mathbf{e}_k$$

for the base vector \mathbf{e}_i in the Cartesian coordinate system. The Voigt notation of vectors and second-order tensors are denoted by bold-face minuscule and majuscule letters like \mathbf{a} and \mathbf{A} , respectively. The MacAuley brackets are defined as $\langle x \rangle = \max(x, 0)$.

2. Phase-field cohesive zone models for multi-physical fracture

In this section the phase-field cohesive zone model (PF-CZM) for purely mechanical fracture is extended to a couple of multi-physics problems including, e.g., thermo-mechanical fracture due to thermal shocks, hydrogen-assisted chemo-mechanical fracture in metals, chemo-thermo-mechanical fracture in early-age concrete and electromechanical fracture in piezoelectric ceramics, etc.

2.1. Fracture in purely mechanical problems

The PF-CZM for fracture in pure mechanics problems is first presented within the framework of the unified phase-field theory for damage and fracture [19–21].

Let $\Omega \subset \mathbb{R}^{n_{\text{dim}}}$ ($n_{\text{dim}} = 1, 2, 3$) be the reference configuration of a cracking solid. The external boundary is denoted by $\partial\Omega \subset \mathbb{R}^{n_{\text{dim}}-1}$ and the outward normal vector by \mathbf{n} . The body forces (per unit volume) \mathbf{b} are distributed within the whole domain Ω and the prescribed tractions

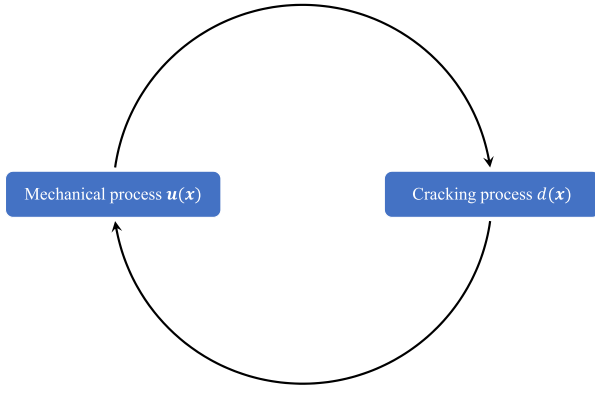


Fig. 1. Damage-mechanical coupling in pure mechanics problems.

t^* are applied to the part of boundary $\partial\Omega_t \subset \partial\Omega$. The resulting deformations of the solid are described by the displacement field $\mathbf{u}(\mathbf{x})$ and the (infinitesimal) strain field $\epsilon(\mathbf{x}) := \nabla^{\text{sym}} \mathbf{u}(\mathbf{x})$, for the symmetric gradient operator $\nabla^{\text{sym}}(\cdot)$ with respect to the spatial coordinate \mathbf{x} . For the well-posedness of the boundary value problem, given displacements \mathbf{u}^* are imposed on the complementary boundary $\partial\Omega_u = \partial\Omega \setminus \partial\Omega_t$.

All the sharp cracks in the solid are collected in the set $S \subset \mathbb{R}^{n_{\text{dim}}-1}$, with the normal vector of the crack surfaces signified by \mathbf{n}_s . In phase-field models for fracture [3,5], the sharp crack S is regularized over a localization band $B \subseteq \Omega$ where the crack phase-field or damage field $d(\mathbf{x}) : B \rightarrow [0, 1]$, satisfying the irreversibility condition $d(\mathbf{x}) \geq 0$, localizes. A phase-field length scale $b > 0$ is introduced to measure the bandwidth — when it vanishes with $b \rightarrow 0$, sharp cracks are recovered. Similar to the displacement field, proper Dirichlet boundary conditions, e.g., $d(\mathbf{x}) = 0$ for elastic domains and $d(\mathbf{x}) = 1$ for pre-defined cracks, can be imposed as well. The external boundary of the localization band B is denoted by ∂B and the outward unit normal vector by \mathbf{n}_B . Note that the localization band is neither prescribed *a priori* nor fixed all along, but rather, it is automatically updated during the crack propagation in accordance with the governing equations for the crack phase-field.

2.1.1. Governing equations

For pure mechanics problems, the phase-field model for fracture is governed by the following damage–displacement coupled formulations

$$\begin{cases} \nabla \cdot \boldsymbol{\sigma} + \mathbf{b} = 0 & \text{in } \Omega \\ \boldsymbol{\sigma} \cdot \mathbf{n} = \mathbf{t}^* & \text{on } \partial\Omega_t \end{cases} \quad (2.1a)$$

$$\begin{cases} \nabla \cdot \mathbf{q} + Q \leq 0 & \text{in } B \\ \mathbf{q} \cdot \mathbf{n}_B \geq 0 & \text{on } \partial B \end{cases} \quad (2.1b)$$

where the stress tensor $\boldsymbol{\sigma}$ is addressed later in Section 2.1.2; the flux vector \mathbf{q} is work conjugate to the damage gradient ∇d , with its divergence balanced by the source term Q , given by

$$\mathbf{q} = \frac{2b}{c_\alpha} G_f \nabla d, \quad Q = -\omega'(d)\bar{Y} - \alpha'(d) \frac{G_f}{c_\alpha b} \quad (2.1c)$$

for the fracture energy (i.e., energy dissipation per unit surface area) G_f , the effective crack driving force \bar{Y} and the scaling constant $c_\alpha = 4 \int_0^1 \sqrt{\alpha(\beta)} d\beta$, respectively. Note that the irreversibility condition $d \geq 0$ has to be explicitly or implicitly imposed to the crack phase-field; see Remark 2.1. As shown in Fig. 1, the mechanical process and the crack phase-field are inter-field strongly coupled.

The above governing equations are characterized by a (monotonically increasing) geometric crack function $\alpha(d) \in [0, 1]$ and a (monotonically decreasing) energetic degradation function $\omega(d) \in [0, 1]$, with the first-order derivatives being $\alpha'(d) := \partial\alpha/\partial d$ and $\omega'(d) := \partial\omega/\partial d$, respectively.

Remark 2.1. In phase-field models for fracture, the damage field $d(\mathbf{x})$ has to fulfill the irreversibility condition $d \geq 0$. A numerically amenable approach is to replace the effective crack driving force \bar{Y} in the phase-field source term (2.1c) by its maximum value H ever reached [62], i.e.,

$$Q = -\omega'(d)H - \alpha'(d) \frac{G_f}{c_\alpha b} \quad \text{with} \quad H = \max\left(\bar{Y}_0, \max_{n \in [0, T]} \bar{Y}_n\right) \quad (2.2)$$

for the effective crack driving force \bar{Y}_n at time t_n . The initial threshold \bar{Y}_0 plays an important role for crack nucleation in solids — materials remain elastic when the crack driving force \bar{Y} does not exceed this critical value \bar{Y}_0 . With the above modification, the phase-field evolution Eq. (2.1b) becomes equalities and the crack irreversibility $d \geq 0$ is guaranteed at all Gaussian points. \square

2.1.2. Constitutive relations

The damage-mechanical coupled governing Eqs. (2.1) need to be supplemented by constitutive relations for the stress $\boldsymbol{\sigma}$ and the effective damage driving force \bar{Y} . Though variationally consistent stress–strain relations can be adopted as in [63], the simplest isotropic one is considered in this work, i.e.,

$$\boldsymbol{\sigma} = \omega(d)\bar{\boldsymbol{\sigma}} = \omega(d)\mathbb{E}_0 : \boldsymbol{\epsilon} \quad (2.3)$$

In the absence of plastic strains, the effective stress tensor $\bar{\boldsymbol{\sigma}}$ is defined by Hooke's elastic relation

$$\bar{\boldsymbol{\sigma}} = \mathbb{E}_0 : \boldsymbol{\epsilon} \quad (2.4)$$

For an initially linear elastic solid, the fourth-order elasticity tensor \mathbb{E}_0 is expressed as

$$\mathbb{E}_0 = \lambda_0 \mathbf{1} \otimes \mathbf{1} + 2\mu_0 \mathbb{I} \quad (2.5)$$

where the Lamé constants of isotropic elasticity, $\lambda_0 := \frac{\nu_0 E_0}{(1-2\nu_0)(1+\nu_0)}$ and $\mu_0 := \frac{E_0}{2(1+\nu_0)}$, are expressed in terms of Young's modulus E_0 and Poisson's ratio ν_0 of the material.

The stress–strain relation (2.3) is unable to discriminate the asymmetric behavior under tension and compression. To address this issue, the following effective crack driving force \bar{Y} is postulated for brittle and quasi-brittle fracture

$$\bar{Y} = \frac{1}{2\bar{E}_0} \langle \bar{\sigma}_1 \rangle^2 \implies \bar{Y}_0 = \frac{f_t^2}{2\bar{E}_0} \quad (2.6)$$

where $\bar{\sigma}_1$ is the first principal value of the effective stress tensor $\bar{\boldsymbol{\sigma}}$; $\bar{E}_0 = \lambda_0 + 2\mu_0$ and f_t are the elongation modulus and the failure strength of the material, respectively.

Note that, though the above constitutive relations are not variationally consistent, they are indeed thermodynamically consistent [64].

Remark 2.2. The Rankine criterion (2.6) incorporates the *strength-based crack nucleation criterion*. That is, cracks nucleate when the maximum effective principal stress $\bar{\sigma}_1$ reaches the failure strength f_t . Note that in some transient multi-physics problems, e.g., hydrogen-assisted cracking in metals and shrinkage induced cracking in early-age concrete, etc., the failure strength f_t is not necessarily a constant and the current value should be used to evaluate the initial threshold (2.6)₂. [65]. \square

2.1.3. Optimal characteristic functions

In accordance with our previous studies [19–21], the following characteristic functions are postulated

$$\begin{cases} \alpha(d) = 2d - d^2 & c_\alpha = \pi \\ \omega(d) = \frac{(1-d)^p}{(1-d)^p + a_1 d \cdot P(d)} & P(d) = 1 + a_2 d + a_3 d^2 \end{cases} \quad (2.7)$$

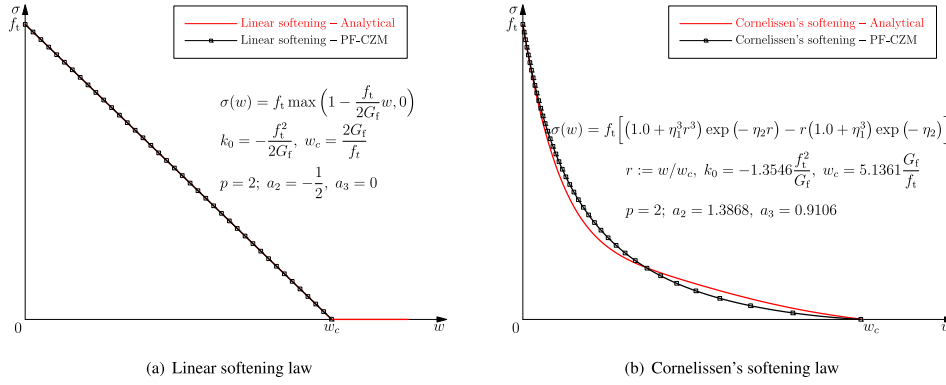


Fig. 2. The target softening curves and the phase-field approximations.

where the parameters $p \geq 2$, $a_1 > 0$, a_2 and a_3 are given by

$$a_1 = \frac{4}{\pi} \cdot \frac{l_{ch}}{b}, \quad a_2 = 2\beta_k^{2/3} - \left(p + \frac{1}{2}\right), \quad a_3 = \begin{cases} 0 & p > 2 \\ \frac{1}{2}\beta_w^2 - (1 + a_2) & p = 2 \end{cases} \quad (2.8)$$

where Irwin's internal length $l_{ch} := \bar{E}_0 G_f / f_t^2$ measures the size of fracture process zone — the smaller it is, the more brittle the material behaves; the ratios β_k and β_w compare the initial slope k_0 and the limit crack opening w_c of the target traction-separation law (TSL) against those of the linear softening curve, i.e.,

$$\beta_k := \frac{k_0}{-\frac{1}{2}f_t^2/G_f} \geq 1, \quad \beta_w := \frac{w_c}{2G_f/f_t} \quad (2.9)$$

For instance, the linear softening law for brittle fracture and the Cornelissen's [66] softening curve for concrete like quasi-brittle solids can be reproduced or approximated as shown in Fig. 2 with the following parameters

$$\begin{cases} \text{Linear softening curve:} & p = 2, a_2 = -\frac{1}{2}, a_3 = 0 \\ \text{Cornelissen's softening curve:} & p = 2, a_2 = 1.3868, a_3 = 0.9106 \end{cases} \quad (2.10)$$

Note that for both brittle and quasi-brittle fracture, the predicted crack patterns, failure modes and global responses are all insensitive to the phase-field length scale parameter, so long as the latter is small enough.

2.2. Fracture in thermo-mechanical problems

In this section, the above PF-CZM is extended to modeling thermo-mechanical fracture as in [42]. To this end, an extra temperature field $T(\mathbf{x})$ is introduced. Correspondingly, the external boundary is split into two parts, i.e., the one $\partial\Omega_h$ with prescribed heat flux h^* and the supplementary one $\partial\Omega_T = \Omega \setminus \partial\Omega_h$ with given temperature T^* .

2.2.1. Governing equations for thermal transfer process

In addition to the damage-mechanical coupled governing Eqs. (2.1), one needs an extra set of partial differentiation equations (PDEs) to describe the heat transfer process

$$\begin{cases} \rho c \dot{T} + \nabla \cdot \mathbf{h} = \Theta^* & \text{in } \Omega \\ \mathbf{h} \cdot \mathbf{n} = h^* & \text{on } \partial\Omega_h \end{cases} \quad (2.11)$$

for the volumetric heat source Θ^* . The heat flux \mathbf{h} is given by Fourier's law

$$\mathbf{h} = -\boldsymbol{\kappa} \cdot \nabla T = -\omega(d) \boldsymbol{\kappa}_0 \cdot \nabla T \quad (2.12)$$

where $\boldsymbol{\kappa}_0 = \kappa_0 \mathbf{1}$ is the second-order isotropic thermal conductivity tensor, with the coefficient κ_0 being constant.

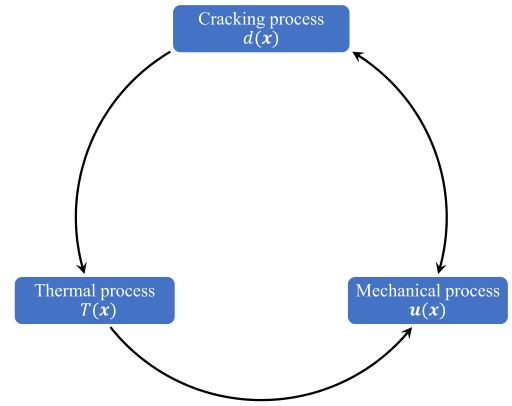


Fig. 3. Thermo-damage-mechanical coupling in thermo-mechanical problems.

2.2.2. Constitutive relations

Due to the thermal expansion, the total strain in the solid allows an additive split

$$\boldsymbol{\epsilon} = \boldsymbol{\epsilon}^m + \boldsymbol{\epsilon}^t \quad (2.13)$$

where $\boldsymbol{\epsilon}^m$ is the mechanical strain; the thermal strain $\boldsymbol{\epsilon}^t$ is assumed to be isotropic and expressed as

$$\boldsymbol{\epsilon}^t = \eta_t (T - T_0) \mathbf{1} \quad (2.14)$$

for the thermal expansion coefficient η_t and the reference temperature T_0 .

Upon the above additive decomposition, the constitutive relations addressed in Section 2.1.2 still applies, except that the effective stress tensor $\bar{\boldsymbol{\sigma}}$ should be modified as

$$\bar{\boldsymbol{\sigma}} = \mathbb{E}_0 : \boldsymbol{\epsilon}^m = \mathbb{E}_0 : (\boldsymbol{\epsilon} - \boldsymbol{\epsilon}^t) \quad (2.15)$$

with the thermal strain excluded.

For the sake of simplicity, it is assumed as in [67,68] that the material mechanical properties during thermal shocks are temperature independent. In this case, as shown in Fig. 3 the thermal transfer process affects the mechanical one but not directly vice versa — the former is affected indirectly by the latter through the “bridging interaction” of the cracking phase-field.

2.3. Fracture in chemo-mechanical problems

In this section, the PF-CZM is extended to modeling the hydrogen-assisted cracking involving chemo-mechanical fracture. To this end, an extra concentration field $C(\mathbf{x})$ is introduced, in addition to the displacement field $\mathbf{u}(\mathbf{x})$ and the crack phase-field $d(\mathbf{x})$. Moreover, the

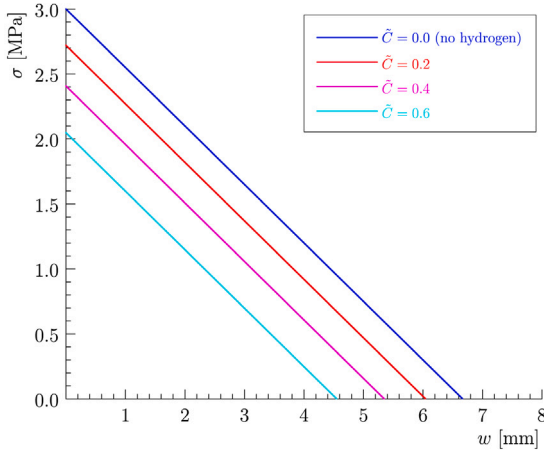


Fig. 4. Hydrogen-dependent linear softening laws with $\beta = 0.89$ in the degradation function (2.20) ($G_f = 10$ N/mm and $f_t = 3.0$ MPa).

external boundary $\partial\Omega$ of the solid is split into one part $\partial\Omega_c$ where the given concentration C^* is imposed and the complementary one $\partial\Omega_f = \partial\Omega \setminus \partial\Omega_c$ through which the flux J^* is prescribed.

2.3.1. Governing equations for hydrogen diffusion

Besides the damage-mechanical coupled governing equations (2.1), one needs an extra set of PDEs to describe the hydrogen diffusion process

$$\begin{cases} \dot{C} + \nabla \cdot \mathbf{J} = 0 & \text{in } \Omega \\ \mathbf{J} \cdot \mathbf{n} = J^* & \text{on } \partial\Omega_f \end{cases} \quad (2.16)$$

for the flux \mathbf{J} given by the modified Fick law [69]

$$\mathbf{J} = -D\nabla C + \frac{DV_H}{RT} C \nabla \sigma_H \quad (2.17)$$

where D is the bulk diffusivity, V_H is the partial molar volume of the impurity, and $\sigma_H := \frac{1}{3} \text{tr} \sigma$ is the hydrostatic stress; $R = 8.314$ J/(mol K) is the universal gas constant, T is the absolute temperature.

2.3.2. Hydrogen-dependent traction-separation laws

As hydrogen-assisted cracking is a localized phenomenon, it is necessary to evaluate the hydrogen coverage (surface concentration) \tilde{C} from the bulk one C . According to [70], this relation is provided by the Langmuir-McLean isotherm [71]

$$\tilde{C} = \frac{C}{C + \exp\left(-\frac{\Delta g_b^0}{RT}\right)} \quad (2.18)$$

where C is given in the unit of impurity mole fraction; Δg_b^0 denotes the Gibbs free energy difference between the adsorbed and bulk standard states. Note that, when the bulk concentration C is low, it is more convenient to be replaced by $5.5 \times 10^{-5} C$ in the unit of wt. ppm (part per million weight).

In the presence of hydrogen, the mechanical properties of metals decrease with increasing hydrogen concentrations. It is assumed in this work that Young's modulus E_0 is not affected, while the failure strength f_t and fracture energy G_f are degraded in such a way that Irwin's internal length l_{ch} is fixed [40]

$$\begin{aligned} f_t(\tilde{C}) &= \sqrt{\varphi(\tilde{C})} f_{t0}, & G_f(\tilde{C}) &= \varphi(\tilde{C}) G_{f0} \\ \Rightarrow l_{ch} &:= \frac{E_0 G_f}{f_t^2} = \frac{E_0 G_{f0}}{f_{t0}^2} = l_{ch0} \end{aligned} \quad (2.19)$$

where f_{t0} , G_{f0} and l_{ch0} represent the failure strength, the fracture energy and Irwin's internal length, respectively, at null hydrogen concentration $\tilde{C} = 0$; the hydrogen degradation functions $\varphi(\tilde{C})$ is simply

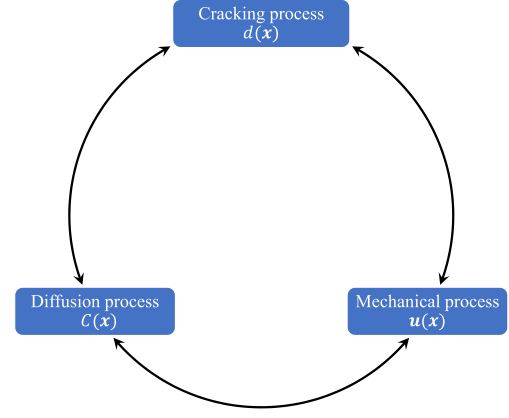


Fig. 5. Chemo-damage-mechanical coupling in chemo-mechanical problems.

expressed in terms of the surface concentration \tilde{C} in the cohesive zone [72]

$$\varphi(\tilde{C}) = 1 - \beta \tilde{C} \quad (2.20)$$

for the coefficient $\beta \in [0, 1]$. Regarding the linear softening, the resulting softening curves for various hydrogen coverage are shown in Fig. 4.

As shown in Fig. 5, for this multi-physics problem, the diffusion, cracking and mechanical processes are inter-field strongly coupled.

2.4. Fracture in chemo-thermo-mechanical problems

In this section, the PF-CZM is extended to the modeling of shrinkage induced cracking in early-age concrete which involves chemo-thermal-mechanical fracture with age effect.

Besides the displacement field $\mathbf{u}(\mathbf{x})$, the phase-field $d(\mathbf{x})$ and the temperature $T(\mathbf{x})$, an extra hydration degree $\tau(\mathbf{x}) \in [0, 1]$ is introduced to describe the hydration process in the solid Ω , i.e., $\tau = 0$ for no hydration while $\tau = 1$ for full hydration [73]. For the thermal boundary conditions, the external boundary is split into three parts, i.e., the one $\partial\Omega_h$ with prescribed heat flux h^* , the one $\partial\Omega_g$ with a convection/radiation coefficient g^* for convection with air of given ambient temperature T_a , and the last one $\partial\Omega_T = \Omega \setminus \partial\Omega_h \setminus \partial\Omega_g$ with prescribed temperature T^* .

2.4.1. Governing equations for the hydration process

In addition to the damage-displacement coupled governing equations (2.1), the temperature field is governed by

$$\begin{cases} \rho c \dot{T} + \nabla \cdot \mathbf{h} = \Theta & \text{in } \Omega \\ \mathbf{h} \cdot \mathbf{n} = h^* + g(T - T_a) & \text{on } \partial\Omega_h \cup \partial\Omega_g \end{cases} \quad (2.21)$$

where ρc is the heat capacity per unit volume.

For hydration in early-age concrete, the volumetric heat release Θ is proportional to the hydration degree rate $\dot{\tau}$ by the potential heat p_∞ , i.e.,

$$\Theta = p_\infty \dot{\tau} \quad \text{with} \quad \dot{\tau} = \omega(d) \psi(\tau) \exp\left(-\frac{E_a}{RT}\right) \quad (2.22)$$

where E_a is the activation energy, and the chemical affinity function [74–76] $\psi(\tau)$ is usually fitted from the experimental data of the isothermal calorimetry [77]. As can be seen, the hydration process is affected by the cracking phase-field.

2.4.2. Constitutive relations

Due to the presence of thermal expansions and hydration induced shrinkage, the total strain of the solid is decomposed as

$$\epsilon = \epsilon^m + \epsilon^t + \epsilon^s \quad (2.23)$$

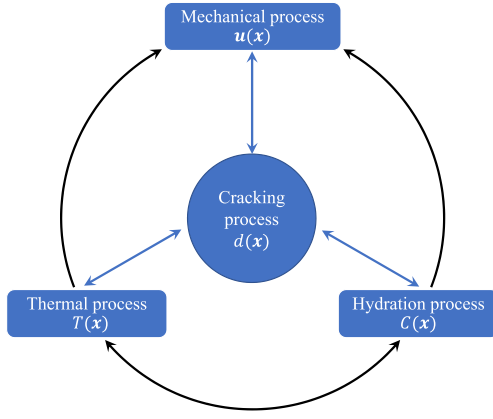


Fig. 6. Chemo-thermo-damage-mechanical coupling in chemo-thermo-mechanical problems.

for the mechanical strain ϵ^m , the thermal strain ϵ^t in Eq. (2.14) and the autogenous shrinkage strain ϵ^s

$$\epsilon^s = -\eta_s \zeta(\tau) \mathbf{1} \quad (2.24)$$

where the coefficient η_s characterizes the autogenous shrinkage through the following truncation function $\zeta(\tau)$

$$\zeta(\tau) = \left\langle \frac{\tau - \tau_0}{\tau_\infty - \tau_0} \right\rangle, \quad \tau_\infty = 1 - \exp\left(-3.3 \frac{w}{c}\right) \quad (2.25)$$

once the hydration degree τ exceeds the threshold τ_0 , with the limit hydration degree τ_∞ expressed in terms of the water-cement ratio w/c of concrete mixture [78].

Upon the above additive decomposition, the constitutive relations presented in Section 2.1.2 still apply with the effective stress tensor $\bar{\sigma}$ modified as

$$\bar{\sigma} = \mathbb{E}_0 : \epsilon^m = \mathbb{E}_0 : (\epsilon - \epsilon^t - \epsilon^s) \quad (2.26)$$

in which both the thermal expansion and autogenous shrinkage are excluded.

2.4.3. Age effect

As hydration evolves, concrete gets hardening and the mechanical properties, i.e., Young's modulus E_0 , the tensile strength f_t and the fracture energy G_f , all increase with the curing age, while Poisson's ratio ν_0 remains almost constant. In this work, the age effect is formulated by [79,80]

$$\begin{cases} E_0(\tau) = E_0^\infty \zeta(\tau) \\ f_t(\tau) = f_t^\infty \zeta(\tau) \\ G_f(\tau) = G_f^\infty \zeta(\tau) \end{cases} \quad (2.27)$$

where the truncation function $\zeta(\tau)$ given in Eq. (2.25) is adopted for the sake of simplicity.

Note that, due to the variations of the mechanical properties, Irwin's characteristic length l_{ch} and the parameter a_1 in Eq. (2.8) also vary. Contrariwise, the other two parameters, a_2 and a_3 , depend only on the specific softening curve and remain unaffected. As shown in Fig. 6, the interdependence of cracking process and thermal/hydration/mechanical processes, or between thermal process and hydration one are considered, while the effects of mechanical process on thermal/hydration ones are indirectly accounted for via the "bridging interactions" through the crack phase-field.

2.5. Fracture in electromechanical problems

Finally let us consider the electromechanical fracture in linear isotropic piezoelectric solids [81]. The primary unknowns consist of

the mechanical displacement field $u(x)$, the crack phase-field $d(x)$ and the electric potential $\phi(x)$. In the infinitesimal range, the electric field $\chi(x)$ is defined by

$$\chi(x) = -\nabla \phi(x) \quad (2.28)$$

with respect to the spatial coordinate x .

2.5.1. Governing equations

For the quasi-static case of interest, the electric potential field ϕ satisfies the following governing equations

$$\begin{cases} \nabla \cdot \theta - \rho_e^* = 0 & \text{in } \Omega \\ \theta \cdot n = -q^* & \text{on } \partial\Omega_q \end{cases} \quad (2.29)$$

where θ is the electric displacement, and ρ_e^* is the electric charge density in the piezoelectric solid. Regarding the electric boundary conditions, the external boundary $\partial\Omega$ is split into one part $\partial\Omega_\phi$ with prescribed electric potential ϕ^* and the other one $\partial\Omega_q$ subjected to given surface charge q^* .

2.5.2. Constitutive relations

In this work, the traction-free and electrically impermeable crack boundary conditions on the faces of a fully softened crack are considered as in [82–85]. Accordingly, the following constitutive equations apply

$$\begin{cases} \sigma = \omega(d) (\mathbb{E}_0 : \epsilon - \mathbb{H}_0^T \cdot \chi) \\ \theta = \omega(d) (\mathbb{H}_0 : \epsilon + \epsilon_0 \cdot \chi) \end{cases} \quad (2.30)$$

for the fourth-order elasticity tensor \mathbb{E}_0 given in Eq. (2.5). The third-order piezoelectric coupling tensor \mathbb{H}_0 and the second-order dielectric tensor ϵ_0 are expressed as

$$\mathbb{H}_0 = c_1 p \otimes \mathbf{1} + c_2 p \otimes p \otimes p + c_3 p \otimes \bar{\otimes} \mathbf{1}, \quad \epsilon_0 = \epsilon_0 \mathbf{1} \quad (2.31)$$

where c_1 , c_2 and c_3 are the axial, lateral and shearing piezoelectric coefficients of the material, respectively; the vector p represents the poling direction due to material polarization under electric fields; ϵ_0 is the dielectric material parameter (i.e., the electric permittivity).

Due to the strong coupling between constitutive relations, the effective crack driving force Eq. (2.6) for purely mechanical fracture needs to be modified. In [81] the following expression is derived

$$\bar{Y} = \frac{1}{2\bar{E}_0} \left(\langle \bar{\sigma}_1 \rangle^2 - c_\chi \chi \langle \bar{\sigma}_1 \rangle \right) \quad (2.32)$$

for the coefficient c_χ

$$c_\chi = p \cdot \mathbb{H}_0 : (n_1 \otimes n_1) = c_1 + (c_2 + c_3) (p \cdot n_1)^2 \quad (2.33)$$

where n_1 is the first principal vector of the effective stress tensor $\bar{\sigma}$ defined in Eq. (2.4); χ is the magnitude of the electric field vector $\chi = \chi p$. Note that the effective crack driving force (2.32) coincides with the purely mechanical counterpart Eq. (2.6) in the absence of electric field, i.e., $\chi = 0$; see [81] for more details.

For this multi-physics problem, the electrical, cracking and mechanical inter-field coupling is shown in Fig. 7.

3. Numerical implementation in COMSOL

In this section, the numerical aspects in implementing the PF-CZM are addressed for various multi-physics problems in COMSOL MULTIPHYSICS. The procedures in COMSOL MULTIPHYSICS mainly include the definition of strong-form governing equations of each involved physical field and the setup of the solver. On the basis of these works, spatial and temporal discretization will be automatically executed according to some built-in standard numerical techniques, i.e., finite element and Euler method, with solving process following to attain equilibrium results. Here we present the module setup for each type of fracture problems and the staggered algorithm for solving non-linear coupling

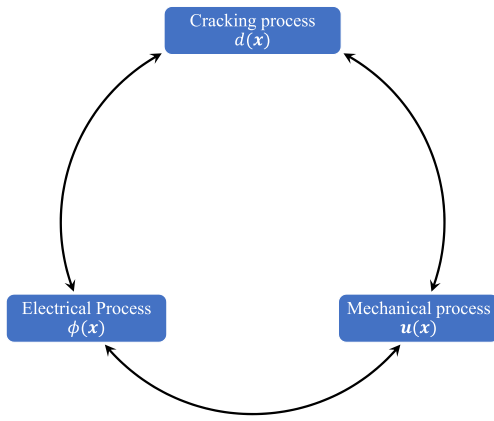


Fig. 7. Electro-mechanical-damage coupling in electromechanical problems.

equations, which promises the feasibility of implementing PF-CZM in COMSOL MULTIPHYSICS.

3.1. Module setup in COMSOL MULTIPHYSICS

Only the governing equations in strong form are needed in COMSOL MULTIPHYSICS. Regarding purely mechanical problems, two basic modules, i.e., SOLID MECHANICS and POISSON'S EQUATION, can be adopted to solve the mechanical displacement u and the crack phase-field d , respectively. For more complex multi-physics problems, extra modules are needed. These topics will be addressed in sequence.

3.1.1. Maximum crack driving force

In the literature, Zhou et al. [60] used the DOMAIN ODES AND DAEs (ordinary differential equations and differential algebraic equations) module to calculate the crack driving force H . However, this strategy compares the nodal thresholds with the crack driving force at the Gaussian points, leading to imprecise results.

Here we abandoned the above strategy and utilize the STATE VARIABLES OF VARIABLE UTILITIES to calculate the crack driving force of a specific Gaussian point at the beginning of each incremental step, i.e.,

$$H = \max[\bar{Y}_0, \max(\bar{Y}_n, \bar{Y})] \quad (3.1)$$

where \bar{Y}_n is the maximum crack driving force achieved until the last increment; \bar{Y} and \bar{Y}_0 are the effective crack driving force and the threshold at current incremental step, respectively.

At the end of current increment, the maximum crack driving force \bar{Y} is updated by

$$\bar{Y} = \max(\bar{Y}_n, \bar{Y}) \quad (3.2)$$

which will be used in the next increment.

3.1.2. Purely mechanical problems

The mechanical sub-problem (2.1a) is implemented by the SOLID MECHANICS module. For the constitutive relation (2.3), a LINEAR ELASTIC MATERIAL model is defined in terms of the user-defined Young's modulus $\omega(d)E_0$ and Poisson's ratio ν_0 , with $\omega(d)$ being the energetic degradation function (2.7). Note that this built-in module in COMSOL MULTIPHYSICS applies to both quasi-static and dynamic problems, with the inertial terms neglected or included. Moreover, proper initial and boundary conditions can be imposed.

Several standard PDEs modules built-in COMSOL MULTIPHYSICS can be used in implementation of the phase-field governing equations (2.1b). Here, the POISSON'S EQUATION module is adopted, in which one needs only

to define the DIFFUSION COEFFICIENT c and SOURCE TERM f as follows

$$\begin{cases} c = \frac{2b}{c_a} G_f \\ f = -\omega'(d)H - \frac{G_f}{c_a b} \alpha'(d) \end{cases} \quad (3.3)$$

for the crack driving force H in Eq. (3.1). Similarly, proper initial and boundary conditions can be applied.

3.1.3. Thermo-mechanical problems

For thermo-mechanical fracture problems, one more module, HEAT TRANSFER IN SOLIDS, is needed to describe the heat conduction process in solids. In this module, three parameters are input, i.e., the THERMAL CONDUCTIVITY $\omega(d)k_0$ for the energetic degradation function $\omega(d)$ given in Eq. (2.7), the DENSITY ρ and the SPECIFIC HEAT c . Moreover, the heat flux applied to $\partial\Omega_c$ and the temperature imposed on $\partial\Omega_T$, together with the initial temperature field, have to be properly considered.

Moreover, in order to account for the thermal strain ϵ^t , the SOLID MECHANICS module needs to be modified a bit. That is, the THERMAL EXPANSION with a SECANT COEFFICIENT η_t is added to the LINEAR ELASTIC MATERIAL model, and the volume reference temperature $T_{\text{ref}} = T_0$ and the temperature T related to the HEAT TRANSFER IN SOLIDS module are also given.

3.1.4. Chemo-mechanical problems

Regarding hydrogen-assisted cracking in metals, as Eq. (2.17) shows, the hydrogen flux J depends on the gradient of the hydrostatic stress $\nabla\sigma_H$. Accordingly, we need to evaluate the hydrostatic stress field σ_H from the known values at the Gaussian points [41]. To this end, the DOMAIN ODES AND DAEs module is adopted as

$$\sigma_H - \text{solid.IIIs}/3 = 0 \quad (3.4)$$

for the built-in variable `solid.IIIs` representing the first invariant of the stress tensor in SOLID MECHANICS module. With the above hydrostatic stress field σ_H , its gradient can be obtained by the differentiation operators with respect to the spatial coordinates in COMSOL MULTIPHYSICS.

The governing equation (2.16) for hydrogen diffusion is implemented through the CONVECTION-DIFFUSION EQUATION (cdeq) module. In particular, the DIFFUSION COEFFICIENT c is set as D in isotropic form, the DAMPING OR MASS COEFFICIENT d_a is chosen to be 1 and the CONSERVATIVE FLUX CONVECTION COEFFICIENT α is given by

$$\alpha = -\frac{DV_H}{RT} \left[\frac{\partial\sigma_H/\partial x}{\partial\sigma_H/\partial y} \right] \quad (3.5)$$

while all the other terms are set as 0 by default. The associated initial and boundary conditions of the hydrogen diffusion process can be properly considered.

As stated in Eq. (2.19), the hydrogen concentration alters the mechanical properties of the material, i.e. the tensile strength f_t and the fracture energy G_f . Therefore, both properties depend on the hydrogen coverage, and the relevant variables in the SOLID MECHANICS module and the POISSON'S EQUATION module need to be modified accordingly.

3.1.5. Chemo-thermo-mechanical problems

In this case, two extra modules, i.e., the HEAT TRANSFER IN SOLIDS module and the DOMAIN ODES AND DAEs module, are employed to deal with the heat conduction and hydration evolution, respectively.

Similar to those for thermo-mechanical problems in Section 3.1.3, three parameters are needed in the HEAT TRANSFER IN SOLIDS module, i.e., the THERMAL CONDUCTIVITY $\omega(d)k_0$, the DENSITY ρ and the SPECIFIC HEAT c . The heat generation $p_\infty \dot{\tau}$ due to hydration is achieved through the built-in HEAT SOURCE. Proper initial and boundary conditions for the thermal process can be imposed.

Evolution of the hydration degree τ is implemented through the DOMAIN ODES AND DAEs module, with Eq. (2.22)₂ being the input and $\tau_0 = 0$ set as the initial value.

Due to the presence of thermal expansion and autogenous shrinkage, the SOLID MECHANICS module needs to be modified a bit. Specifically, the THERMAL EXPANSION with the SECANT COEFFICIENT η_t is added for the thermal strain, and the following user-defined EXTERNAL STRAIN is input for the autogenous shrinkage strain

$$\epsilon_{\text{ext}} = \begin{bmatrix} \epsilon^s & 0 & 0 \\ 0 & \epsilon^s & 0 \\ 0 & 0 & \epsilon^s \end{bmatrix} \quad \text{with} \quad \epsilon^s = -\eta_s \left\langle \frac{\tau - \tau_0}{\tau_\infty - \tau_0} \right\rangle \quad (3.6)$$

according to Eq. (2.24).

The age effect given in Section 2.4.3 needs to be properly considered. That is, the mechanical properties of the material in the SOLID MECHANICAL module, the DOMAIN ODEs AND DAEs module and the POISSON'S EQUATION module, are all dependent on the hydration degree τ .

3.1.6. Electromechanical problems

The implementation of the PF-CZM for electromechanical fracture needs an extra ELECTROSTATICS module. Moreover, the PIEZOELECTRIC EFFECT MULTIPHYSICS module is adopted to connect the SOLID MECHANICS module with the ELECTROSTATICS one so that the coupling terms in piezoelectric materials are considered automatically. Note that the stress in Voigt notation for piezoelectric materials in COMSOL MULTIPHYSICS is represented as $\sigma = [\sigma_{xx}, \sigma_{yy}, \sigma_{zz}, \sigma_{yz}, \sigma_{xz}, \sigma_{xy}]^T$.

In the SOLID MECHANICAL module, the PIEZOELECTRIC MATERIAL model is used, with the coupled constitutive Eqs. (2.30) given in the STRESS-CHARGE FORM

$$\begin{cases} \sigma = \mathbb{E}\epsilon - \mathbb{H}^T \chi \\ \theta = \mathbb{H}\epsilon + \epsilon_0 \chi \end{cases} \quad (3.7)$$

where the elasticity matrix \mathbb{E} is input as usual in terms of the Lamé constants $\lambda = \omega(d)\lambda_0$ and $\mu = \omega(d)\mu_0$, and the coupling matrix \mathbb{H} is given by

$$\mathbb{H} = \begin{bmatrix} H_{111} & H_{122} & H_{133} & H_{123} & H_{113} & H_{112} \\ H_{211} & H_{222} & H_{233} & H_{223} & H_{213} & H_{212} \\ H_{311} & H_{322} & H_{333} & H_{323} & H_{313} & H_{312} \end{bmatrix} \quad (3.8)$$

with the components $H_{ijk} = \omega(d)[c_1 p_i \delta_{jk} + c_2 p_i p_j p_k + \frac{1}{2} c_3 (p_j \delta_{ik} + p_k \delta_{ij})]$ satisfying the condition $H_{ijk} = H_{ikj}$. Moreover, the dielectric tensor ϵ_0 is defined by the isotropic user-defined RELATIVE PERMITTIVITY ϵ_0 .

Owing to the MULTIPHYSICS PIEZOELECTRIC EFFECT module, the ELECTROSTATICS module is automatically implemented from the PIEZOELECTRIC MATERIAL model of the SOLID MECHANICS module.

The POISSON'S EQUATION module for the crack phase-field is identical to that for the purely mechanical problems, with the only exception that the effective crack driving force \bar{Y} calculated according to Eq. (2.32). Note that, in order to determine the eigenvalue and the associated principal vector of the effective stress tensor $\bar{\sigma}$, the MATRIX DIAGONALIZATION module can be employed.

3.2. Spatial and temporal discretization

With the governing equations in strong form and constitutive relations properly implemented as above, COMSOL MULTIPHYSICS automatically converts them to the equivalent weak form using the weighted residual method. These governing equations in weak form are then solved by the finite element discretization in spatial domain and finite difference discretization in temporal one.

In order to reduce computational cost, if necessary the whole computational domain is divided into two sub-domains: the sub-domain \mathcal{B}^h where the cracks are expected to present and the remainder $\Omega^h \setminus \mathcal{B}^h$ which is free of damage. The element size h within the sub-domain \mathcal{B}^h is sufficiently smaller than the phase-field length scale b such that an accurate estimation of the fracture energy can be guaranteed [5]. From our previous experiences [19,20], the mesh size $h \leq b/5$ is accurate enough. Those element nodes belonging to the sub-domain \mathcal{B}^h have

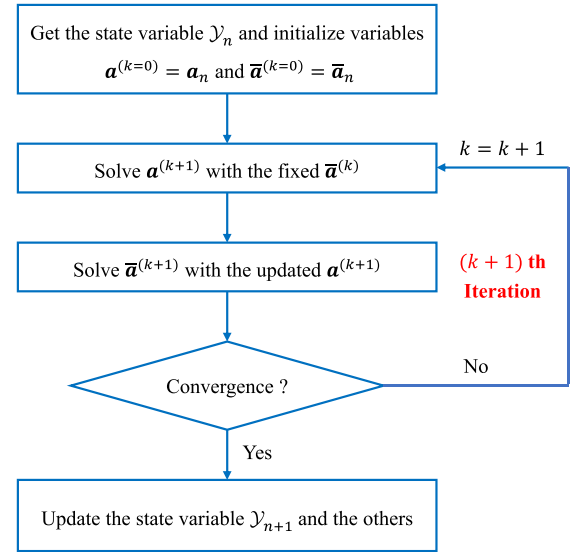


Fig. 8. Flow chart of the staggered algorithm in solving the governing equations of purely mechanical fracture problems.

one more degree of freedom (dof), i.e., the crack phase-field, than those within the sub-domain $\Omega^h \setminus \mathcal{B}^h$ with no damage.

The finite element spatial discretization yields a system of algebraic or ordinary differential equations which are strongly nonlinear and usually solved in an incremental procedure. That is, the time interval $[0, t]$ of interest is split into N increments $[t_n, t_{n+1}]$ for $n = 0, 1, 2, \dots, N-1$. For a typical time increment $[t_n, t_{n+1}]$ of size $\Delta t := t_{n+1} - t_n$, the rate of a specific state variable, if it is presented, is approximated by the backward Euler method. The resulting algebraic equations in residual form are then solved in an iterative manner, with all the state variables known at t_n .

3.3. Solution strategies

In order to solve the nonlinear algebraic governing equations in residual-form, either a monolithic algorithm or a staggered one, both available in COMSOL MULTIPHYSICS, can be employed.

For the monolithic algorithm, the nonlinear governing equations in residual-form are linearized with respect to all the involved nodal unknowns so that they are solved simultaneously. If such a monolithic algorithm works as reported in [65,86] for the BFGS quasi-newton one, the final solution converges rapidly. However, only the standard Newton-Raphson based monolithic algorithm is available in COMSOL MULTIPHYSICS, which is notoriously not robust enough for strongly inter-field coupled problems [6].

Regarding the staggered algorithm, the nonlinear governing equations in residual-form are solved in an alternating manner. That is, the nodal unknowns are split into several groups containing a single or several field variables. Only the field variables in one group are solved at one time with those in the others fixed, and then the field variables in the second group are solved alternately, and so on. The above procedure is repeated until the final solution converges. Though the convergence rate is low [60,64], such a staggered algorithm is proved to be very robust.

3.3.1. Purely mechanical problems

For purely mechanical fracture, the flow chart of the staggered algorithm is shown in Fig. 8. More specifically,

- Solve the nodal displacements $\mathbf{a}^{(k+1)}$ from the mechanical sub-problem with the damage dofs fixed as the solution $\bar{\mathbf{a}}^{(k)}$ of the

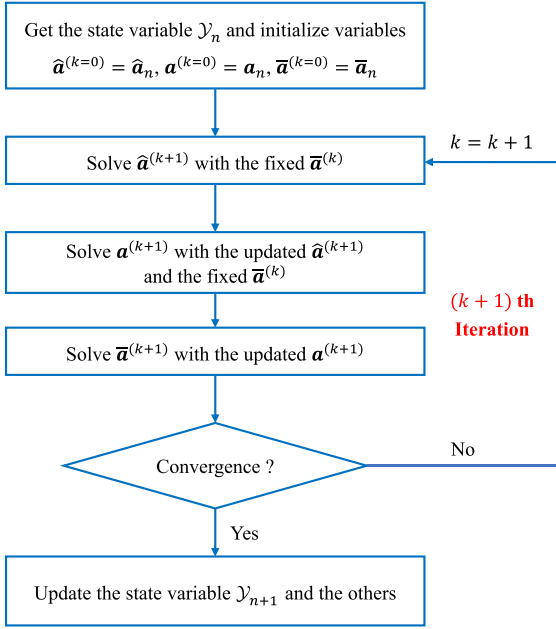


Fig. 9. Flow chart of the staggered algorithm in solving the governing equations of thermo-mechanical fracture problems.

previous k th iteration. For the isotropic constitutive relation (2.3), this mechanical sub-problem is linear in terms of the nodal displacements \mathbf{a} and the solution converges in a single iteration.

- Solve the nodal crack phase-field dofs $\bar{\mathbf{a}}^{(k+1)}$ from the damage sub-problem with the updated nodal displacements $\mathbf{a}^{(k+1)}$. As the governing equations in residual form is nonlinear, usually a couple of iterations are needed for the convergence.

3.3.2. Thermo-mechanical problems

For thermo-mechanical fracture problems, the governing equations in residual form are split into the thermal, mechanical and damage sub-problems which are solved alternately as shown in Fig. 9. In each incremental step,

- Solve the nodal temperature dofs $\hat{\mathbf{a}}^{(k+1)}$ from the thermal sub-problem, with the nodal damage dofs fixed as the values $\bar{\mathbf{a}}^{(k)}$ obtained from the previous iteration. Note that the nodal displacement field does not directly affect the heat transfer process.
- Solve the nodal displacement dofs $\mathbf{a}^{(k+1)}$ from the mechanical sub-problem, with the updated nodal temperature dofs $\hat{\mathbf{a}}^{(k+1)}$ and the damage dofs $\bar{\mathbf{a}}^{(k)}$ fixed.
- Solve the nodal damage dofs $\bar{\mathbf{a}}^{(k+1)}$ from the damage sub-problem with the updated nodal displacements $\mathbf{a}^{(k+1)}$.

3.3.3. Chemo-mechanical problems

For the hydrogen-assisted cracking involving chemo-mechanical fracture, the coupled governing equations are split into the mechanical sub-problem, the hydrogen diffusion one, the one related to the hydrostatic stress, and the damage one. These sub-problems are collected into two groups, i.e., the damage sub-problem and the second one including all the others, which are solved alternately as shown in Fig. 10.

- Solve the nodal displacement, hydrogen concentration and hydrostatic stress dofs $(\mathbf{a}^{(k+1)}, \bar{\mathbf{a}}^{(k+1)}, \hat{\mathbf{a}}^{(k+1)})$ simultaneously from the mechanical, hydrogen diffusion and hydrostatic stress sub-problems, with the damage dofs fixed as the solution $\bar{\mathbf{a}}^{(k)}$ of the previous iteration.

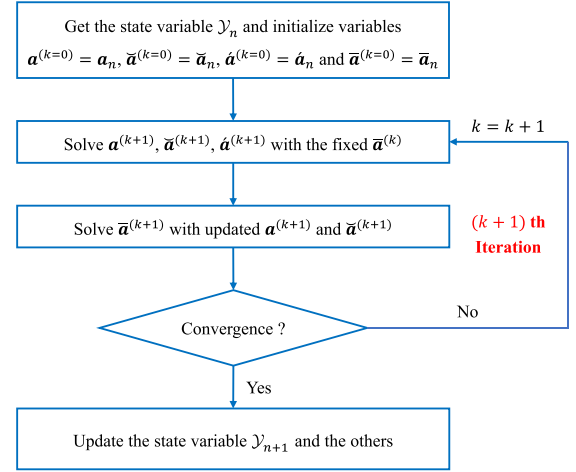


Fig. 10. Flow chart of the staggered algorithm in solving the governing equations of chemo-mechanical fracture problems.

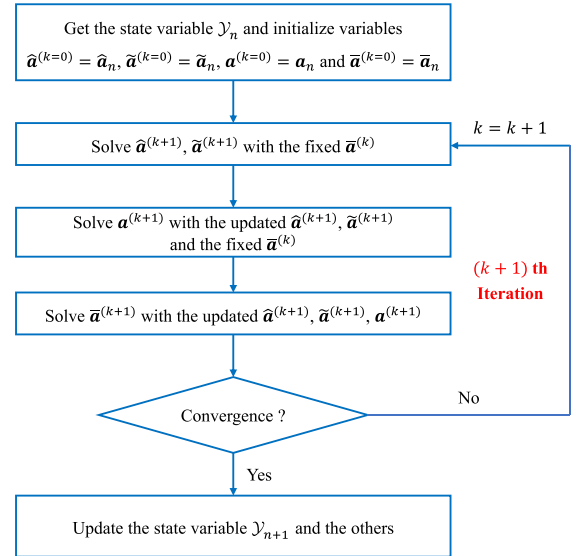


Fig. 11. Flow chart of the staggered algorithm in solving the governing equations of chemo-thermo-mechanical fracture problems.

- Solve the damage dofs $\bar{\mathbf{a}}^{(k+1)}$ from the damage sub-problem with the updated nodal displacement and hydrogen concentration dofs $(\mathbf{a}^{(k+1)}, \hat{\mathbf{a}}^{(k+1)})$. Note that the hydrostatic stress field does not interact directly with the damage sub-problem.

3.3.4. Chemo-thermo-mechanical problems

As shown in Fig. 11, for shrinkage induced cracking in early-age concrete the governing equations in residual form are split into the chemo-thermal, mechanical and damage sub-problems, and are solved alternately.

- Solve the nodal temperature and hydration degree dofs $(\hat{\mathbf{a}}^{(k+1)}, \bar{\mathbf{a}}^{(k+1)})$ simultaneously from the chemo-thermal sub-problem, with the damage dofs fixed as the solution $\bar{\mathbf{a}}^{(k)}$ of the previous iteration. Note that the displacement field does not affect directly the chemo-thermal sub-problem.
- Solve the nodal displacements $\mathbf{a}^{(k+1)}$ from the mechanical sub-problem with the updated temperature and hydration degree dofs $(\hat{\mathbf{a}}^{(k+1)}, \bar{\mathbf{a}}^{(k+1)})$ and the fixed damage dofs $\bar{\mathbf{a}}^{(k)}$ of the previous iteration.

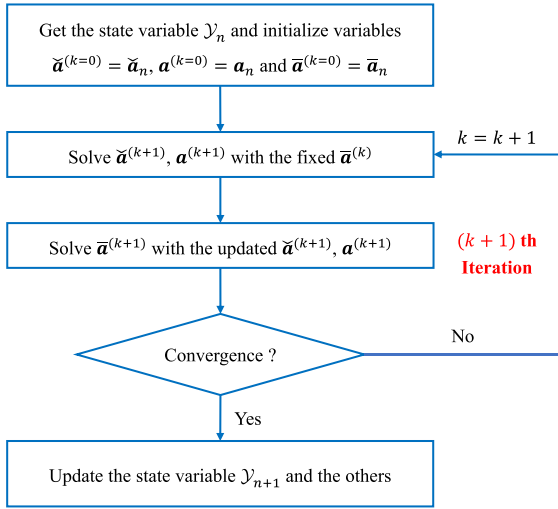


Fig. 12. Flow chart of the staggered algorithm in solving the governing equations of electromechanical fracture problems.

- Solve the nodal damage dofs $\bar{\mathbf{a}}^{(k+1)}$ from the damage sub-problem with the updated unknowns $(\tilde{\mathbf{a}}^{(k+1)}, \tilde{\mathbf{a}}^{(k+1)}, \mathbf{a}^{(k+1)})$.

3.3.5. Electromechanical problems

For electromechanical fracture in linear piezoelectric ceramics, the coupled governing equations in residual form are split into the piezoelectric sub-problem related to the nodal displacements and electric potentials, and the damage sub-problem. The solution flow chart is depicted in Fig. 12.

- Solve the nodal electric potential and displacement dofs $(\tilde{\mathbf{a}}^{(k+1)}, \mathbf{a}^{(k+1)})$ simultaneously from the piezoelectric sub-problem, with the nodal damage dofs fixed as the solution $\bar{\mathbf{a}}^{(k)}$ of the previous iteration.
- Solve the nodal damage dofs $\bar{\mathbf{a}}^{(k+1)}$ from the damage sub-problem with the updated nodal electric potentials and displacements $(\tilde{\mathbf{a}}^{(k+1)}, \mathbf{a}^{(k+1)})$.

3.4. Convergence criterion

In each incremental step, the aforementioned solving procedures are repeated until the solution converges within a specific tolerance. In COMSOL MULTIPHYSICS, the following commonly adopted convergence criteria are available for the staggered algorithm:

- One-pass criterion [62]: This option is activated in COMSOL MULTIPHYSICS by setting a single global iteration. As no global convergence is checked, this scheme is robust and has been widely adopted [31,34]. However, extremely small time increments (usually less than $\sim 10^{-5}$ for the quasi-static case) have to be used. Importantly, this scheme may slow down crack propagation, sometimes leading to imprecise or erroneous numerical results.
- Solution-based criterion [3,60,64,87]: This criterion checks the solution tolerance of the nodal dofs between two consecutive iterations, i.e., $\|\mathbf{z}^j\|$ and $\|\mathbf{z}^{j+1}\|$ for the iteration numbers j and $j+1$, with $\|\cdot\|$ being an appropriate scaling norm (e.g., L_2 -norm) of the nodal solution vector \mathbf{z} .
- Residual-based criterion [57,86,88,89]: This criterion checks the residuals of all the governing equations. It is commonly included in those commercial finite element software packages like ABAQUS and COMSOL MULTIPHYSICS.

Both the solution-based criterion and the residual-based one give numerically precise solutions even if large incremental sizes ($\sim 10^{-2}$ for the quasi-static case) are adopted. Therefore, they are well suitable for the phase-field cohesive zone modeling of fracture in the multiphysics problems.

3.5. Indirect displacement control

As localized failure is inevitably accompanied with material softening induced snap-backs, path-following techniques like the arc-length control are useful to track the whole equilibrium path in the numerical simulation. In this case, the applied forces or displacements are not given *a priori*, but rather, they are parametrized by a scaling parameter ϑ to the (known) reference nodal forces \mathbf{f}^* or nodal displacements \mathbf{a}^*

$$\mathbf{f}^{\text{ext}} = \vartheta \mathbf{f}^* + \mathbf{f}_0^*, \quad \mathbf{a} = \vartheta \mathbf{a}^* + \mathbf{a}_0^* \quad (3.9)$$

where \mathbf{f}_0^* and \mathbf{a}_0^* are both constant vectors representing the initial values and can be zeros. Practically, the case of either prescribed forces ($\mathbf{f}^* \neq \mathbf{0}$ and $\mathbf{a}^* = \mathbf{0}$) or prescribed displacements ($\mathbf{f}^* = \mathbf{0}$ and $\mathbf{a}^* \neq \mathbf{0}$) can be considered.

In order to determine the scaling parameter ϑ , an extra constraining equation is supplemented. Though there exist several path-following strategies dealing with snap-backs, in this work the indirect displacement control or local arc-length method proposed by [90] is considered, with the path-following constraint expressed as

$$r_\vartheta(\mathbf{a}) = l - \mathbf{S}^T \mathbf{a} = 0 \quad (3.10)$$

where the loading procedure is controlled by the pseudo-time parameter l ; \mathbf{S} is the selection vector [91] as stated in Remark 3.1. The augmented unknowns (\mathbf{a}, ϑ) are then solved from the mechanical sub-problem and the constraint (3.10) for a given increment Δl ; see [64] for the details. This scheme makes it possible to simulate servo-controlled loads frequently used in experimental tests.

In COMSOL MULTIPHYSICS, the indirect displacement control with the constrain (3.10) is implemented through the GLOBAL EQUATION in the SOLID MECHANICS module. It connects the prescribed external forces in the POINT LOAD or external displacements in the PRESCRIBED DISPLACEMENT with the given pseudo-time parameter l . As will be shown later, it is rather robust even when highly localized failure is observed.

Remark 3.1. In the case of indirect displacement control, the contributing dofs have to be selected *a priori* such that the pseudo-time parameter l is monotonically increasing. They can be either identified from experimental test or selected heuristically. In the numerical examples presented later in this work, the crack mouth opening or sliding displacements, i.e., CMOD or CMSD, is considered. In this case, the selection vector is given in the form $\mathbf{S} = \{0, \dots, 0, 1, 0, \dots, 0, -1, 0, \dots, 0\}^T$, where the locations with non-zero values correspond to the normal or tangential displacement dofs of the nodes at opposite sides of the crack mouth. \square

4. Representative numerical examples

In this section, a couple of numerical examples, regarding fracture in purely mechanical, thermo-mechanical, chemo-mechanical, chemo-thermo-mechanical and electromechanical problems, are presented. The numerical performances of the PF-CZM are demonstrated. Both brittle fracture with linear softening law and quasi-brittle failure with Cornelissen et al. [92] softening law are considered. Note that in order to resolve the gradient of the crack phase-field, the phase-field length scale b should be taken as small as possible. Fortunately, in the PF-CZM the length scale b affects neither the crack pattern nor the global response. In practice, the upper bound $b \leq \frac{1}{3}l_{\text{ch}}$ is usually considered [86] for the sake of numerical robustness.

The PF-CZM and the numerical implementation addressed in Section 3 applies to both 2-D and 3-D problems, though plane stress is

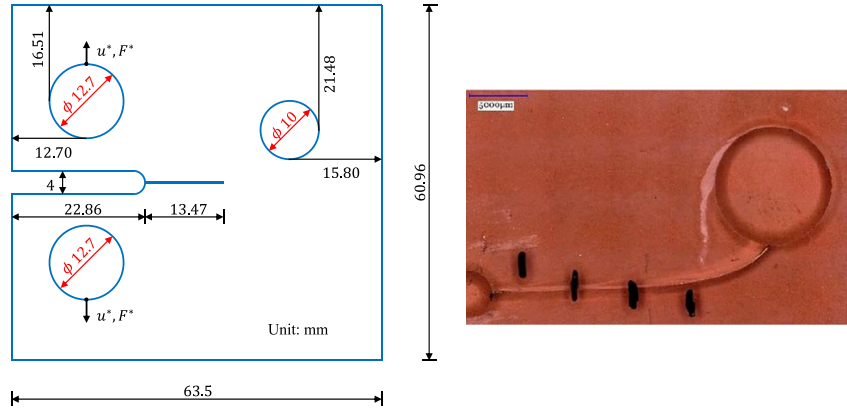


Fig. 13. Mixed-mode fracture of a PMMA plate: Geometry and loading conditions (left) and the experimentally observed crack path (right).

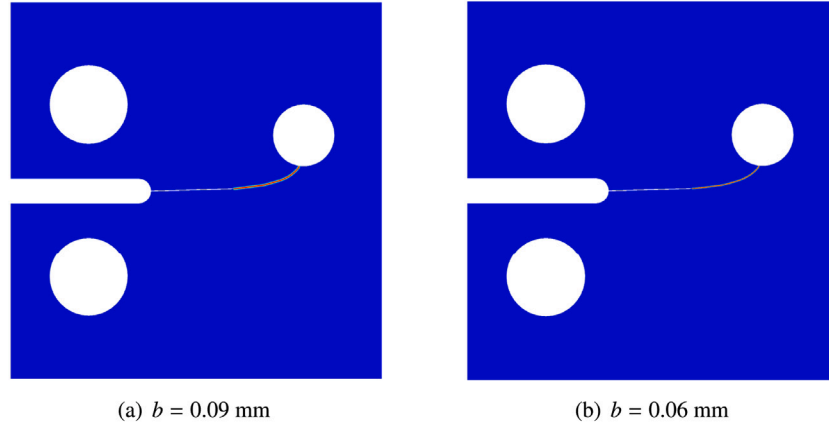


Fig. 14. Mixed-mode fracture of a PMMA plate: Numerically predicted crack patterns.

assumed in most examples if not specified explicitly. Quadrilateral bilinear elements are used to discretize the computational domain. Fine meshes are used within those sub-domains containing potential crack paths while coarse ones are used elsewhere in order to relieve computational burdens. However, in all examples the crack is allowed to nucleate at any place and propagate arbitrarily without knowing the path *a priori*.

All simulations are carried out using the aforesaid implementation of the PF-CZM in COMSOL MULTIPHYSICS; see <https://github.com/jiayingwu/pfczm-comsol> for the source codes and example files. The default solution-based convergence criterion is adopted for the STAGGERED SOLVER and the FREE TIME INCREMENT option is used to solve the nonlinear equations with an adaptive time stepping. A computer workstation with Intel(R) Core(TM) i7-7700HQ CPU@2.80 GHz and 512 GB RAM using 26 cores was used in parallel computation. The computation times for all the presented examples are summarized in Section 4.6.

4.1. Purely mechanical fracture

Let us first consider two purely mechanical fracture problems, one being the brittle fracture of a PMMA specimen and the other being the quasi-brittle failure of a notched concrete beam. They are used to validate the implementation of the PF-CZM in COMSOL MULTIPHYSICS and the indirect displacement control for highly localized failure.

4.1.1. Mixed-mode fracture of a PMMA plate

A PMMA plate of mixed-mode fracture was reported in Pham et al. [93]. The geometry of the specimen and the loading conditions are depicted in Fig. 13. Distinct from the standard compact tension of mode-I fracture, a pre-defined sharp crack of length 13.47 mm and

a circular hole of diameter 10 mm at the upper-right domain were introduced to induce mixed-mode (I + II) failure of the specimen.

In the simulation, the material properties reported in the test [93], i.e., $E_0 = 2.98 \times 10^3$ MPa, $\nu = 0.35$, $f_t = 50$ MPa and $G_f = 0.285$ N/mm, are adopted. The linear softening curve (2.10)₁ is used for this brittle fracture. Two different phase-field length scale parameters, $b = 0.09$ mm and $b = 0.06$ mm, much less than Irwin's characteristic length $l_{ch} = 0.387$ mm, are considered.

The numerically predicted crack patterns are shown as Fig. 14. As can be seen, though the localization bandwidths vary for different length scale parameters, both predictions almost coincide and match the experimentally observed crack path fairly well — due to the asymmetry induced by the upper-right hole, the crack path deviates from the horizontal line and gradually turns upward to the hole, exhibiting typical characteristics of mixed-mode fracture.

Fig. 15 presents the predicted load-CMOD curves. As expected, the phase-field length scale parameter does not affect the overall global responses. In particular, though the post-peak behavior exhibit some discrepancies, the ascending branch and the peak load reported by the test data are both well captured.

4.1.2. Single-edge notched concrete beam test

The single-edge notched beam reported in Arrea and Ingraffea [94] is considered as a good benchmark to verify the mixed-mode fracture of concrete. As shown in Fig. 16, the beam is of dimensions 1322 mm \times 306 mm \times 156 mm, with a notch of sizes 14 mm \times 82 mm \times 156 mm at the bottom. Two concentrated loads of proportionality, i.e., $0.13F^*$ and F^* , were exerted on the top of the beam while the bottom is simply supported.

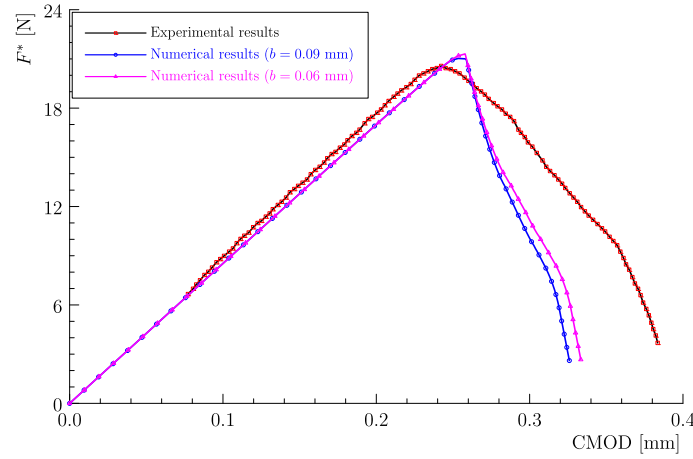


Fig. 15. Mixed-mode fracture of a PMMA plate: Load-CMOD curves.

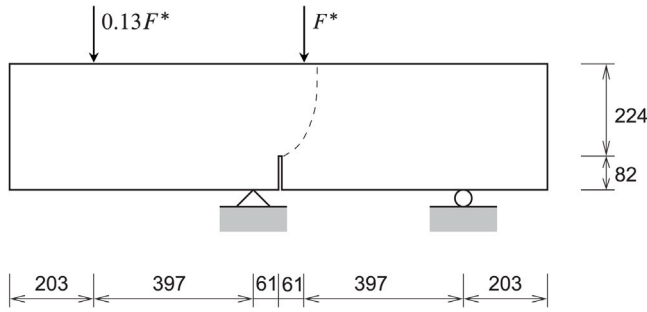


Fig. 16. Single-edge notched concrete beam test: geometry boundary and loading conditions.

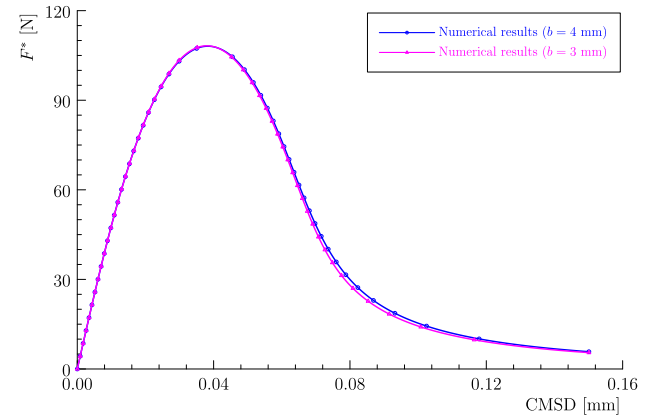


Fig. 18. Single-edge notched concrete beam test: Numerically predicted load-CMSD curves.

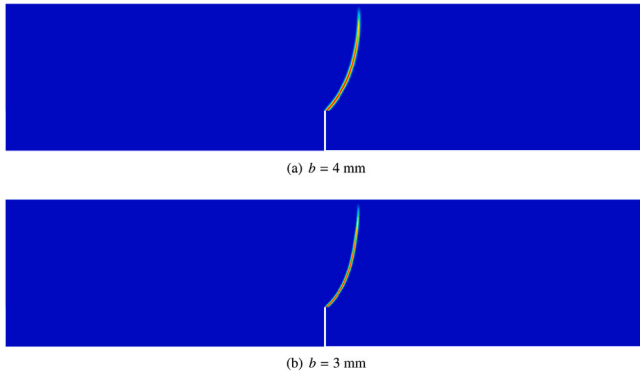


Fig. 17. Single-edge notched concrete beam test: Numerically predicted crack paths.

In the simulation, the material properties are taken from [64,95], i.e., $E_0 = 2.88 \times 10^4$ MPa, $\nu_0 = 0.18$, $f_t = 2.8$ MPa and $G_f = 0.1$ N/mm. The Cornelissen et al. [92] softening curve (2.10)₂ is used for this quasi-brittle failure. Two length scale parameters $b = 4$ mm and $b = 3$ mm, which are much less than Irwin's characteristic length $l_{ch} = 382.7$ mm, are considered. As the load was applied by a pair of prescribed external forces of proportionality, it is inconvenient to use the direct displacement control. To address this issue, the indirect displacement control in terms of the crack mouth sliding displacement (CMSD) is used.

The numerically predicted crack paths are depicted in Fig. 17. As expected, the crack nucleates at the notch and propagates along a curved trajectory upwards to the right hand side of the point where

the force F^* is applied. Moreover, though the diffuse crack band width is proportional to the length scale b , the crack pattern is unaffected.

The predicted load-CMSD curves are shown in Fig. 18. Note that the comparison against the experimental result is unavailable, since the later is available. As can be seen, the overall global response is insensitive to the phase-field length scale as before.

4.2. Thermo-mechanical fracture: Quenching test of a ceramic plate

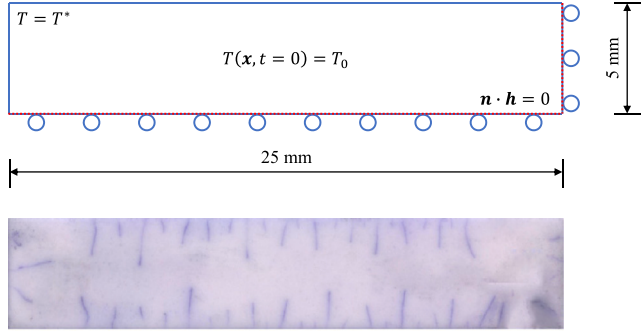
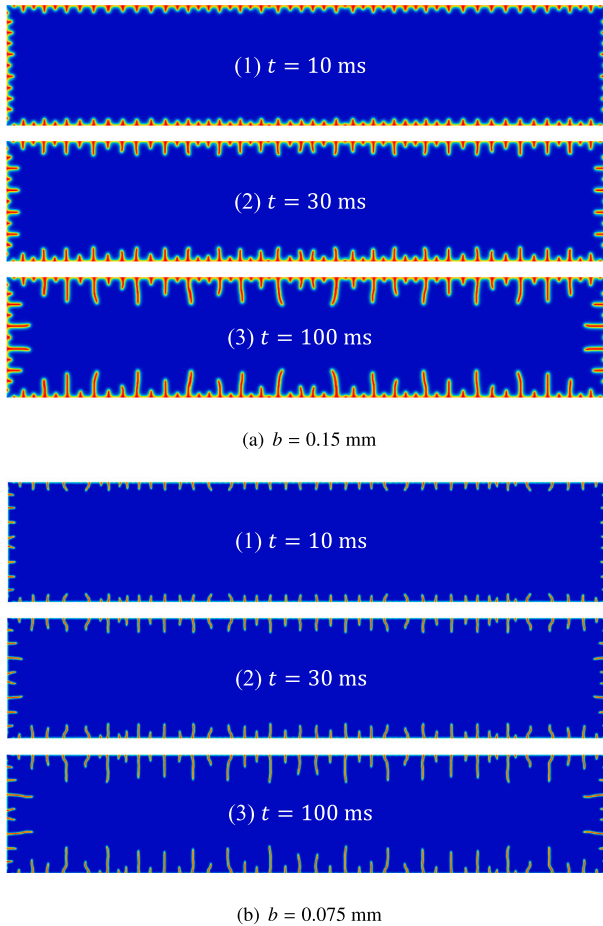
In this section, the quenching test of ceramic plates reported in Jiang [96] is considered. As depicted in Fig. 19 (top), a ceramic plate of dimensions 50 mm \times 10 mm \times 1 mm (in the figure, only one quarter of the specimen is depicted due to symmetry) was heated to a certain temperature T_0 and then dropped into a water bath of 20 °C. After being dropped for 10 min, the ceramic plate was removed from the bath and dyed with blue ink after drying such that the cracks could be observed as in Fig. 19 (bottom). This problem has been widely analyzed in the literature [29,42,97–99]. Here the aim is to validate the applicability of the PF-CZM to thermo-mechanical fracture and its implementation in COMSOL MULTIPHYSICS.

In the simulation the adopted boundary conditions are shown in Fig. 19 (top). Namely, the horizontal displacement on the right edge and the vertical one on the bottom edge are constrained. Due to the symmetry of the heat flux on the plate, an adiabatic condition is assumed on the right and bottom edges, while the Dirichlet boundary

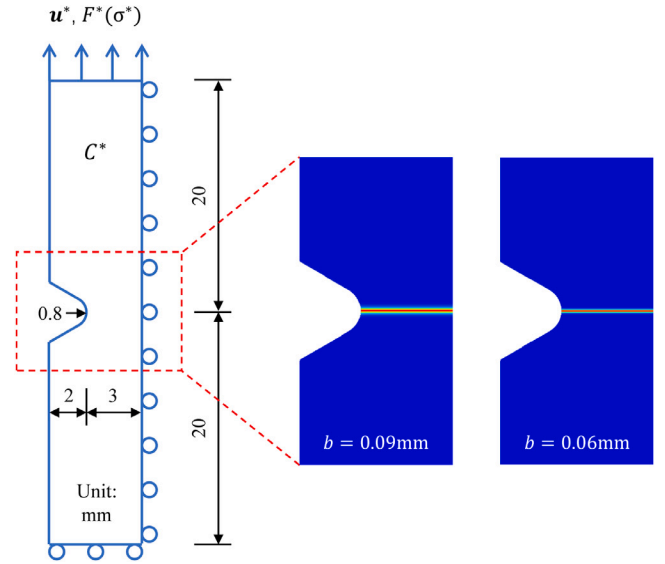
Table 1

Quenching test of a heated ceramic plate: Material parameters.

Material parameters	Values	Material parameters	Values
E_0	370 GPa	η_t	$7.5 \times 10^{-6} \text{ K}^{-1}$
ν_0	0.3	ρ	3980 kg/m ³
f_t	180 MPa	κ_0	31 W/(m K)
G_f	42.47 J/m ²	c	880 J/(kg K)

**Fig. 19.** Quenching test of a heated ceramic plate: Numerical model with geometry and applied boundary conditions (top) and experimentally observed crack pattern (bottom).**Fig. 20.** Quenching test of a heated ceramic plate: Numerically predicted crack patterns for various phase-field length scale parameters.

condition with the temperature 20 °C of water bath is applied to the remaining boundaries [29].

**Fig. 21.** Cylindrical bar with a notch of arc shape under various hydrogen concentrations: Geometry and boundary conditions (left) and the numerical crack paths with different length scale parameters (right).

The model properties are taken from [96,98,100] and summarized in Table 1. All these material properties are assumed to be constant since the temperature-dependent test data are rather limited. Only the results of the initial temperature $T_0 = 300 \text{ °C}$ are presented in this work, and the other cases are referred to [42]. The linear softening curve (2.10)₁ is used for this brittle fracture. Two phase-field length scale parameters, $b = 0.15 \text{ mm}$ and $b = 0.075 \text{ mm}$, are considered. Due to thermal shock, a small time increment $\Delta t = 0.1 \text{ ms}$ is used in the simulation.

The predicted crack patterns of the whole plate shown in Fig. 20 are obtained by symmetrizing and superposing the results of a quarter. The agreement between the numerical prediction and the experimentation observation is fairly well. As can be seen, initially a series of small cracks nucleate at the edges of the plate; with the continuous drop of the temperature, some cracks stop growing while others continue propagating further; eventually, the cracks are distributed with relatively equal spacing which is not affected by the phase-field length scale parameter b .

4.3. Chemo-mechanical fracture: Hydrogen-assisted cracking in metals

In this section, a notched cylindrical bar under traction and different corrosion environments [101] is considered. As shown in Fig. 21 (left), the AISI 4135 steel bar is of radius 5 mm and length 40 mm, with a circumferential notch of root radius 0.8 mm. During the test, the specimens were vertically restrained at the bottom edge and loaded by prescribed a vertical displacement at the top edge. Before loaded, the specimens were pre-charged such that the prescribed hydrogen concentrations range from 0.2 to 2.3 wt. ppm. This example is a good benchmark to validate the PF-CZM for hydrogen-assisted cracking in metals and the implementation in COMSOL MULTIPHYSICS.

The material properties taken from [101,102] are listed in Table 2. In the simulations, the linear softening curve in Eq. (2.10) is used for this brittle fracture.

Let us first compare the numerical predictions given by 2D and 3D simulations. The notched cylindrical bar under a prescribed corrosive concentration $C^* = 1.5 \text{ wt. ppm}$ is considered by 2D axisymmetric and full 3D simulations, respectively. The phase-field length scale $b = 0.1 \text{ mm}$ is adopted in both cases. Regarding the 3D analysis, only one eighth of the bar with proper boundary conditions is modeled, resulting

Table 2

Cylindrical bar with a notch of arc shape under various hydrogen concentrations: Material parameters.

Material parameters	Values	Material parameters	Values
E_0	210 GPa	D	$3.8 \times 10^{-11} \text{ m}^2/\text{s}$
ν_0	0.3	β	0.94
f_t	7400 MPa	V_H	$2 \times 10^{-6} \text{ m}^3/\text{mol}$
G_f	64 kJ/m ²	Δg_b^0	30 kJ/mol

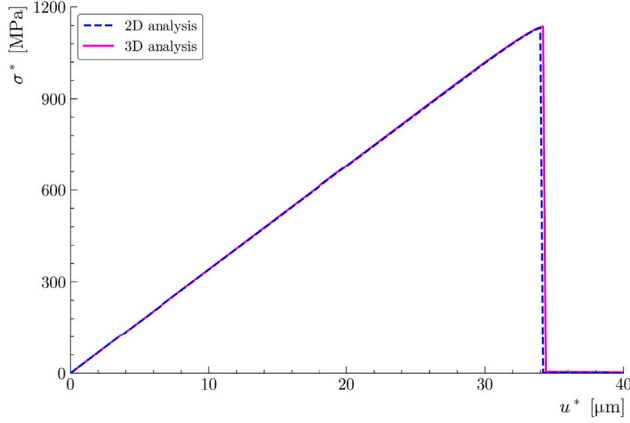


Fig. 22. Cylindrical bar with a notch of arc shape: Comparison of stress–displacement curves given by 2D and 3D simulations.

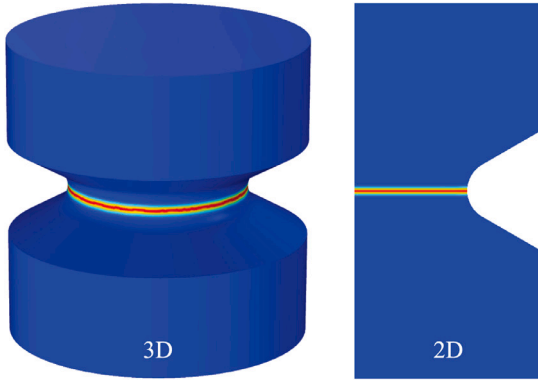


Fig. 23. Cylindrical bar with a notch of arc shape: Comparison of the predicted damage profiles from 2D and 3D simulations.

in a mesh discretization of around 450,000 8-node hexahedron (H8) elements.

Fig. 22 presents the numerically predicted stress–displacement curves. As can be seen, the 2D and 3D simulations give almost identical results. The crack patterns shown in Fig. 23 also confirm this conclusion. That is, both simulations predict identical crack pattern that nucleates from the notch tip and propagates towards the symmetric axis. As it is capable of reproducing the global response and crack pattern with much less degrees of freedom and computational cost, 2D simulations with proper boundary conditions are adopted in this work.

In order to study whether the proposed PF–CZM for coupled chemo-mechanical fracture is insensitive to the phase-field length scale, two cases with $b = 0.09 \text{ mm}$ and $b = 0.06 \text{ mm}$ are considered. A constant hydrogen concentration C^* is applied to all the external boundaries together with an initial uniform distribution of $C_0(x) = C^*$ in the whole bar. Axisymmetric state is assumed in all the simulations.

Fig. 21 (right) shows the crack patterns of the specimen for various phase-field length scale parameters. As can be seen, the crack nucleates at the tip of the pre-defined notch and then propagates quickly to the

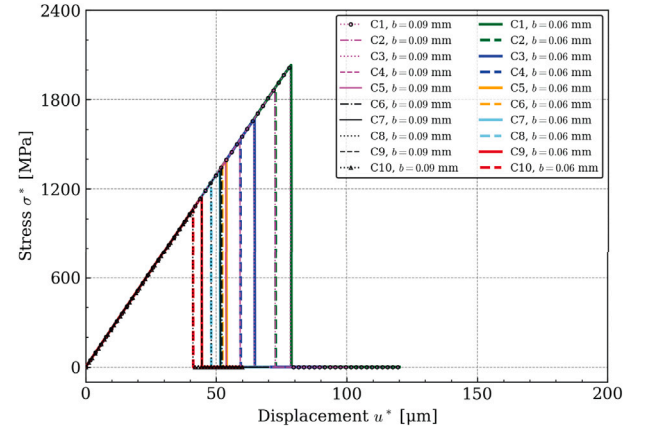


Fig. 24. Cylindrical bar with a notch of arc shape under various hydrogen concentrations: Numerical stress–displacement curves.

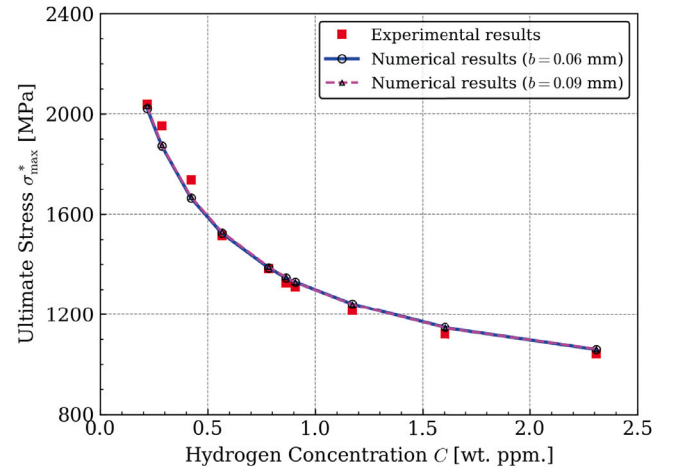


Fig. 25. Cylindrical bar with a notch of arc shape under various hydrogen concentrations: Comparison of the peak stresses against test data.

right, resulting in abrupt drops of the load–displacement curves depicted in Fig. 24. As expected, neither the crack pattern nor the global load–displacement response under various hydrogen concentrations is affected by the phase field length scale.

In order to compare against the experimental results quantitatively, we extract the peak stress by dividing the maximum force by the cross sectional surface area of the specimen at the notch. As shown in Fig. 25, the agreement between the numerical predictions from the PF–CZM and the test data is rather satisfactory. In particular, the degradation trend of the peak stress with increasing hydrogen concentration is well captured.

4.4. Chemo-thermo-mechanical fracture: Shrinkage induced cracking in early-age concrete

In order to validate the PF–CZM for chemo-thermo-mechanical fracture and its implementation in COMSOL MULTIPHYSICS, let us next consider the ring test of early-age concrete reported in [103]. As shown in Fig. 26, the specimen is a circular cement ring of thickness 75 mm, with the outer and inner diameters being 450 mm and 300 mm, respectively. A couple of gauges were attached to the inner steel ring so that evolution of the strain can be monitored. Its abrupt drop represents release of those stresses exerted by the concrete specimen and complete failure of the outer cement ring.

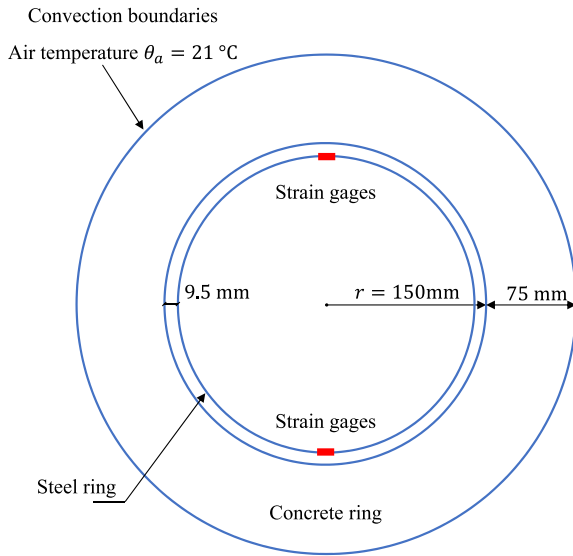


Fig. 26. Restrained concrete ring test: Specimen geometry and environment conditions.

The mechanical properties are taken from [103,104], i.e., $E_{0\infty} = 3.5 \times 10^4$ MPa, $\nu_0 = 0.2$, $f_{t\infty} = 5.29$ MPa and $G_{f\infty} = 0.1$ N/mm, and the other model parameters related to hydration process are summarized in Table 3. The Cornelissen et al. [92] softening curve (2.10)₂ is used for this quasi-brittle failure, and two phase-field length scale parameters, i.e., $b = 5$ mm and $b = 2.5$ mm, are considered.

As young concrete gradually becomes mature with hydration, on the one hand, the volume of concrete autogenously shrinks due to chemical reaction, and on the other hand, heat release of hydration and transfer with the environment lead to initial expansion and eventual shrinkage of concrete. The resulting deformations are restrained by the inner steel ring so that tensile stresses develop along the circumference of the concrete ring. Once the circumferential tensile stress exceeds the continuously increasing mechanical strength, crack nucleation occurs. As can be seen from the numerically predicted evolution of the crack phase-field shown in Fig. 27, initially micro-cracks are uniformly distributed on the inner edge of the cement specimen when the circumferential tensile stress exceeds the strength; as hydration evolves, the shrinkage develops while the mechanical strength also increases, resulting in slow crack propagation; with the shrinkage growing further, one predominant crack propagates quickly and eventually penetrates through the specimen, leading to final failure of the structure. As expected, the phase-field length scale affects only the diffusive crack bandwidth, but the failure mode is unaffected.

The numerical predictions of the strain evolution curves of the inner steel ring are compared against the experimental result in Fig. 28. As can be seen, evolution of the strain is well predicted by the PF-CZM. In particular, the instant when crack propagates quickly and stresses in concrete are released, manifested by the abrupt drop of the compressive stress and strain in the inner steel ring, is captured fairly well. Moreover, the phase-field length scale parameter has negligible effects on the numerical prediction. This property is of great importance for predicting quantitatively the cracking process and fracturing-resistance of early-age concrete.

4.5. Electromechanical fracture: Mixed-mode failure of piezoelectric ceramic beams

Finally, the three-point bending tests of piezoelectric beams under mixed-mode failure reported in [105] is presented to validate the PF-CZM for electromechanical fracture and its implementation in COMSOL.

Table 3

Restrained concrete ring test: Material parameters.

Material parameters	Values	Material parameters	Values
w/c	0.3	τ_{∞}	0.637
τ_0	0.05	E_a	45730 J/mol
η_s	4.5×10^{-4}	p_{∞}	117840 kJ/m ³
η_t	10.0×10^{-6} K ⁻¹	κ_0	2.8 W/(K m)
ρc	2400 kJ/(K m ³)	g	8 W/(K m ²)

Table 4

Mixed-mode failure in three-point bending ceramics beams under electric fields: Material parameters.

Material parameters	Values	Material parameters	Values
E_0	83162 MPa	ϵ_0	6×10^{-9} C/(V m)
ν_0	0.35886	c_1	-6.98 N/(V m)
f_t	55 MPa	c_2	-6.06 N/(V m)
G_f	7 J/m ²	c_3	16.00 N/(V m)

MULTIPHYSICS. Not only the qualitative crack patterns but also the quantitative global responses are compared against the available experimental data.

As shown in Fig. 29, the dimensions of the specimen are 19.1 mm \times 9 mm \times 5.1 mm, and the polarization is placed along the 19.1 mm length direction. A pre-defined notch of sizes 0.46 mm \times 4 mm is introduced perpendicular to the poling direction. Though three different eccentricities of the notch were reported in [105], here only the case of $e = 4$ mm is considered and the interested readers are referred to [81] for other cases. The specimen is loaded mechanically by a vertical downward displacement and electrically by imposing a zero electric potential $\phi = 0$ on the left edge and a non-zero one $\phi = \phi^*$ at the right edge. Five distinct average electric fields, i.e., $\bar{\chi} = -\phi^*/L_0 = \{-5.0, -2.5, 0, 5.0, 10.0\}$ kV/cm, are studied.

The material properties listed in Table 4 are adopted, which are typical for the PZT-4 piezoelectric ceramics [105]. The linear softening law (2.10)₁ is used for this very brittle piezoelectric solid and two distinct phase-field length scale parameters, i.e., $b = 0.030$ mm and $b = 0.045$ mm, are considered.

The numerically predicted evolution of the crack phase-field is shown in Fig. 30. As can be seen, in all cases the mixed-mode failure mode is exhibited as expected. Moreover, the phase-field length scale affects only the diffusive crack bandwidth, while the failure mode is unaffected at all.

Fig. 31 presents the numerical crack paths for various applied electrical fields. Interestingly, a negative electric field retards crack propagation while a positive one facilitates it. This trend is consistent with the experimental findings [105] and other numerical results [31].

The numerical predictions of load-displacement curves are depicted in Fig. 32(a). As can be seen, all the specimens exhibit rather brittle failure and the load-displacement curves drop abruptly due to the rapid crack propagation under the prescribed loading conditions. In all cases, the overall global is not influenced by the phase-field length scale parameter. As shown in Fig. 32(b), the experimentally observed failure strengths of piezoelectric ceramics are captured fairly well — a positive electrical field decreases the fracture load while a negative one improves it.

4.6. Summation of computation time

In Table 5 the computation times of all the previous examples are summarized. Dependent upon whether the problem is multi-physically coupled and the involved degrees of freedom, the computational time ranges from about 1.5 to 48 h which is practically acceptable. In particular, the computational cost of a multi-physically coupled problem is generally higher than that of a purely mechanical one.

Table 5

Computational durations for each numerical example under both purely mechanical and multi-physical circumstances.

Physical fields	Material	Computational time (larger b)	Computational time (smaller b)
Purely mechanical	PMMA	~ 3.0 h	~ 7.0 h
Purely mechanical	Concrete	~ 1.5 h	~ 2.0 h
Coupled thermo-mechanical	Ceramics	~ 10.0 h	~ 25.0 h
Coupled chemo-mechanical	Metal	~ 1.3 h	~ 3.0 h
Coupled chemo-thermo-mechanical	Concrete	~ 6.0 h	~ 14.0 h
Coupled electro-mechanical	Ceramics	~ 20.0 h	~ 48.0 h

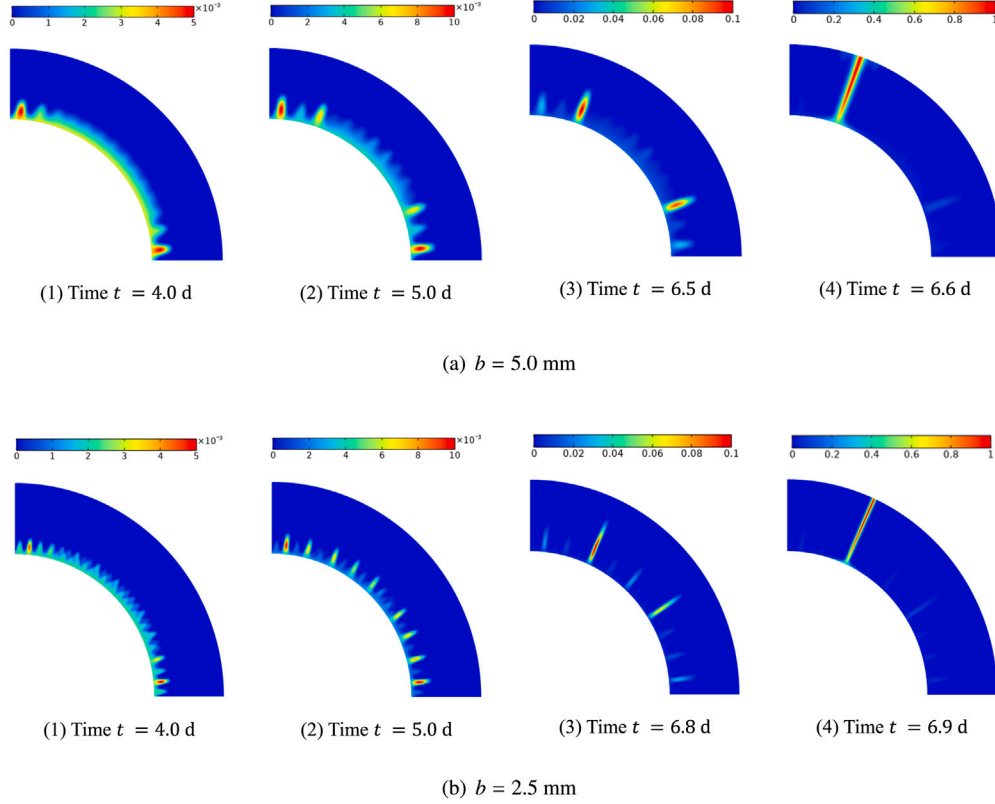


Fig. 27. Restrained concrete ring test: Evolution of the crack phase-field at various time instants for different length scale parameters.

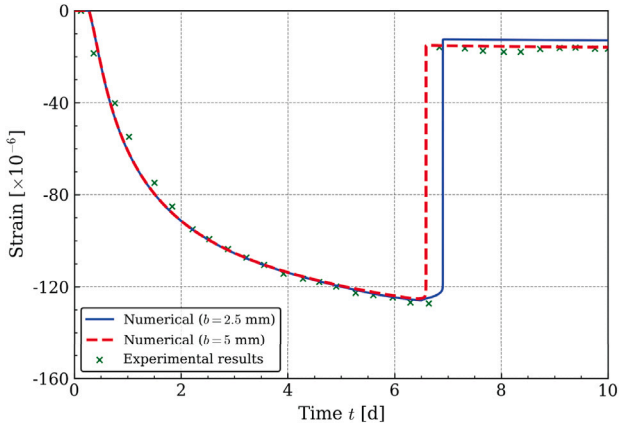


Fig. 28. Restrained concrete ring test: Strain evolution curves of the inner steel ring.

5. Conclusions

This work addresses systematically extensions of the phase-field cohesive zone model (PF-CZM) to brittle fracture and quasi-brittle failure in multi-physics problems and the implementation in COMSOL MULTIPHYSICS. Due to the intrinsic multi-field coupling property and the modular structures of the PF-CZM, its theoretical extension to multi-physics problems is straightforward. Specifically, besides the damage-mechanical coupled governing equations and the corresponding constitutive relations for purely mechanical problems, the following enhancements are needed:

- Thermo-mechanical fracture (thermally induced cracking in ceramics): An extra set of PDEs is introduced to describe the heat transfer process, with the thermal conductivity coefficient is affected by the crack phase-field; mechanically, the thermal strain is excluded from the total one when defining the effective mechanical stress;
- Chemo-mechanical fracture (hydrogen-assisted cracking in metals): An extra set of PDEs is introduced to describe the diffusion process, with the hydrogen flux dependent on the hydrostatic stress (which is related to the strain and the crack phase-field),

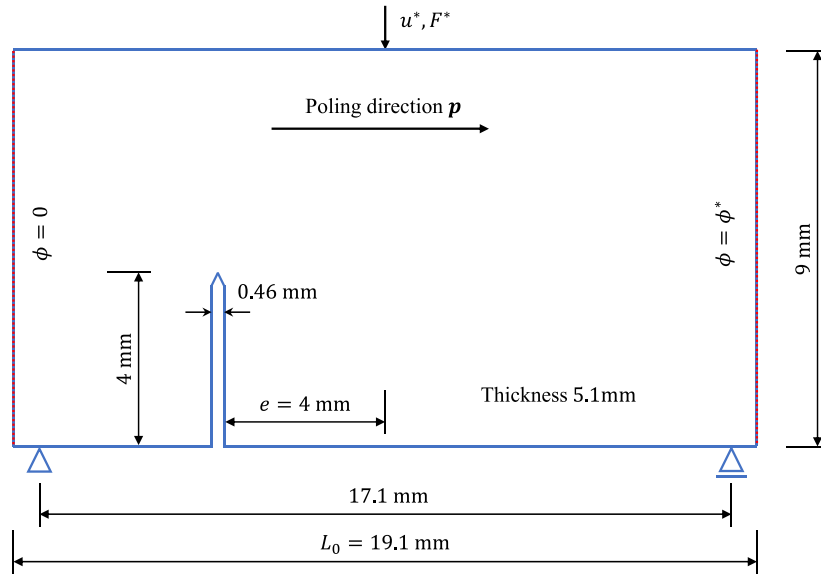


Fig. 29. Mixed-mode failure in three-point bending ceramics beams under electric fields: Geometry and applied conditions.

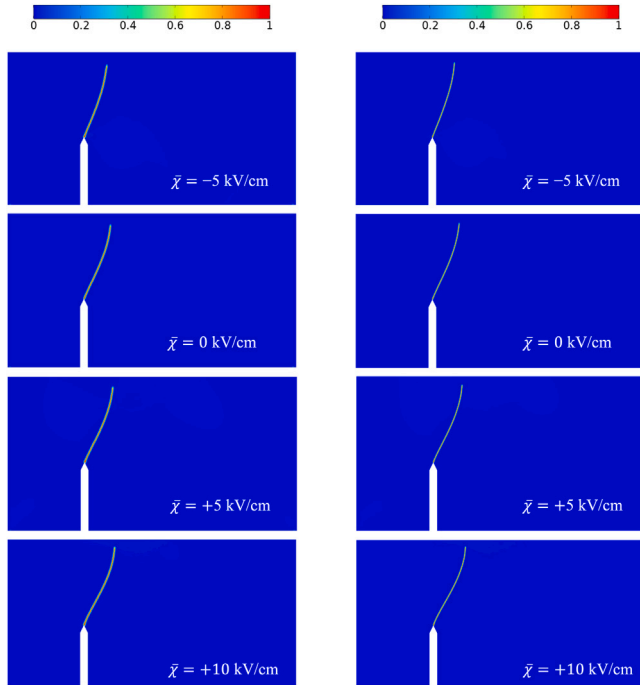


Fig. 30. Mixed-mode failure in three-point bending ceramics beams under electric fields: Evolution of the crack phase-field for $b = 0.045$ mm (left) and $b = 0.030$ mm (right).

and the mechanical properties are degraded by the hydrogen concentration;

- Chemo-thermo-mechanical fracture (shrinkage induced cracking in early-age concrete): An extra set of PDEs for the heat transfer process and one ODE for the hydration process are introduced, with the thermal conductivity coefficient and hydration rate both affected by the crack phase-field; mechanically, the thermal and autogenous shrinkage strains are excluded from the total one in defining the effective mechanical stress, and the age effect (i.e., the hydration-dependent mechanical properties) are also considered;

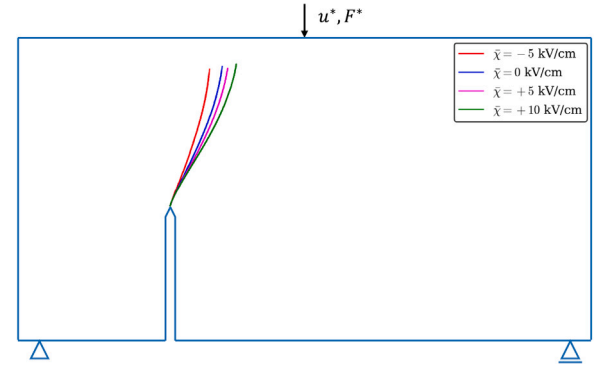


Fig. 31. Mixed-mode failure in three-point bending ceramics beams under electric fields: Crack paths under various average electric fields.

- Electro-mechanical fracture (cracking in piezoelectric solids): An extra set of PDEs is introduced to describe the electric field; moreover, the electromechanical constitutive relations are inter-field coupled, and the purely mechanical contribution is adopted as the effective crack driving force.

Fracture in other multi-physics problems can be similarly considered, with the effect of the crack phase-field on other processes properly accounted for.

For various multi-physics problems, the governing equations in strong form and constitutive relations are then numerically implemented in COMSOL MULTIPHYSICS through some built-in modules. In particular,

- The crack irreversibility condition is dealt with by the introduction of the maximum effective driving force and implemented by the STATE VARIABLES of VARIABLE UTILITIES.
- The mechanical sub-problem is implemented by the SOLID MECHANICS module with the LINEAR ELASTIC MATERIAL model, and the damage sub-problem by the POISSON'S EQUATION module.
- The thermal sub-problem is implemented by the HEAT TRANSFER IN SOLIDS module, and the THERMAL EXPANSION with a SECANT COEFFICIENT is added to the LINEAR ELASTIC MATERIAL model of the SOLID MECHANICS module.

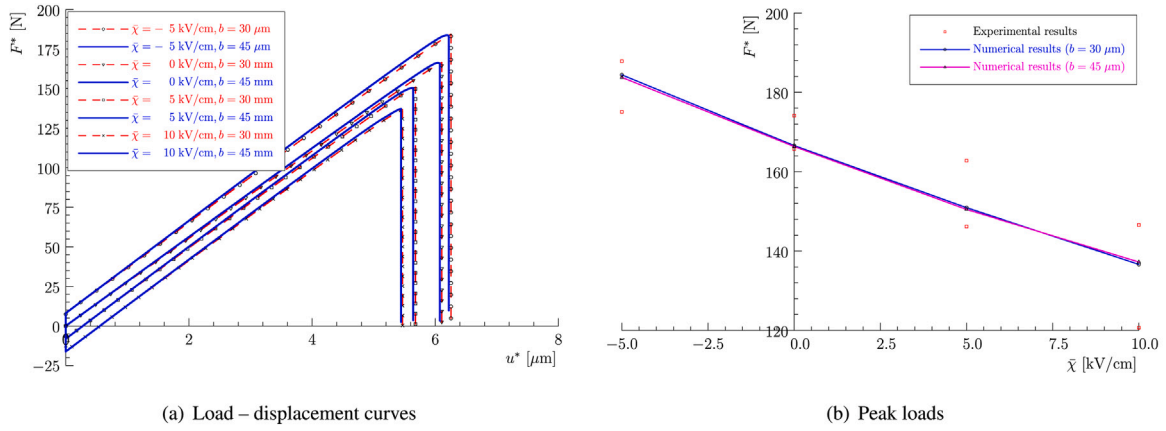


Fig. 32. Mixed-mode failure in three-point bending ceramics beams under electric fields: Predicted load-displacement curves and peak loads.

- The hydrogen diffusion sub-problem is implemented by the CONVECTION-DIFFUSION EQUATION (cdeq) module, and the hydrostatic stress by the DOMAIN ODES AND DAEs module to evaluated its gradient.
- The hydration evolution sub-problem is also implemented by the DOMAIN ODES AND DAEs module, with the autogenous shrinkage strain by the user-defined EXTERNAL STRAIN in the LINEAR ELASTIC MATERIAL model of the SOLID MECHANICS module.
- The electric effect in piezoelectric ceramics is implemented by the ELECTROSTATICS module. Moreover, the PIEZOELECTRIC EFFECT MULTI-PHYSICS module is needed to connected the SOLID MECHANICS module with the ELECTROSTATICS module.
- The indirect displacement control useful for tracking the equilibrium path in localized failure can be implemented by the GLOBAL EQUATION in the SOLID MECHANICS module.

Once the above modules are properly implemented, the governing equations in weak form and the resulting equilibrium equations in residual form are readily solved by the staggered algorithm. That is, the involved field variables are split into several groups and solved iteratively until a specific solution- or residual-based criterion is reached.

A couple of representative benchmark examples are presented to verify the PF-CZM for fracture in multi-physics problems and the numerical implementation. As in the purely mechanical counterpart, the PF-CZM applies to both brittle fracture and quasi-brittle failure even under multi-physically coupled situations. Moreover, in all examples the predicted crack patterns and global responses are insensitive to the phase-field length scale. With the simple and efficient implementation in COMSOL MULTIPHYSICS, the PF-CZM is promising for the modeling of fracture in other more involved multi-physics problems.

Declaration of competing interest

The authors declare that they have no known competing financial interests or personal relationships that could have appeared to influence the work reported in this paper.

Acknowledgments

This work is supported by National Natural Science Foundation of China (52125801; 51878294), State Key Laboratory of Disaster Reduction in Civil Engineering, China (SLDRCE20-01), National Key Laboratory of Shockwave and Denotation Physics, China (JCKYS2020212016), and Guangdong Provincial Key Laboratory of Modern Civil Engineering Technology, China (2021B1212040003) to the second author (J.Y. Wu).

Appendix. Thermodynamic formulation for the hydrogen-assisted fracture

Let us recall the hydrogen-assisted fracture discussed in Section 2.3. For such a coupled chemo-mechanical problem, the principle of virtual work is expressed as

$$\int_{\Omega} (\boldsymbol{\sigma} : \nabla^{\text{sym}} \delta \mathbf{u} + \mathbf{q} \cdot \nabla \delta d - Q \delta d + \dot{C} \delta \mu - \mathbf{J} \cdot \nabla \delta \mu) dV = \int_{\Omega} \mathbf{b} \cdot \delta \mathbf{u} dV + \int_{\partial \Omega_t} \mathbf{t}^* \cdot \delta \mathbf{u} dS - \int_{\partial \Omega_f} \mathbf{J}^* \delta \mu dS \quad (\text{A.1})$$

where μ represents the chemical potential driving the hydrogen flux and the other symbols have been previously introduced. Application of the Gaussian divergence theorem to Eq. (A.1) yields

$$\underbrace{\int_{\Omega} (\nabla \cdot \boldsymbol{\sigma} + \mathbf{b}) \cdot \delta \mathbf{u} dV - \int_{\partial \Omega_t} (\boldsymbol{\sigma} \cdot \mathbf{n} - \mathbf{t}^*) \cdot \delta \mathbf{u} dS}_{\text{Mechanical process}} + \underbrace{\int_{\Omega} (\nabla \cdot \mathbf{q} + Q) \delta d dV - \int_{\partial \Omega} \mathbf{q} \cdot \mathbf{n} \delta d dS}_{\text{Cracking process}} - \underbrace{\int_{\Omega} (\dot{C} + \nabla \cdot \mathbf{J}) \delta \mu dV + \int_{\partial \Omega_f} (\mathbf{J} \cdot \mathbf{n} - \mathbf{J}^*) \delta \mu dS}_{\text{Diffusion process}} = 0 \quad (\text{A.2})$$

from which the governing Eqs. (2.1) and (2.16) can be derived.

For an isothermal coupled chemo-mechanical process, the Clausius-Duhem inequality reads

$$\begin{aligned} \mathcal{D} &= \int_{\Omega} \mathbf{b} \cdot \dot{\mathbf{u}} dV + \int_{\partial \Omega_t} \mathbf{t}^* \cdot \dot{\mathbf{u}} dS - \int_{\partial \Omega_f} \mathbf{J}^* \dot{\mu} dS - \int_{\Omega} \dot{\psi} dV \\ &= \int_{\Omega} \boldsymbol{\sigma} : \dot{\boldsymbol{\epsilon}} dV + \int_{\Omega} (\mathbf{q} \cdot \nabla \dot{d} - Q \dot{d}) dV \\ &\quad + \int_{\Omega} (\dot{C} \mu - \mathbf{J} \cdot \nabla \mu) dV - \int_{\Omega} \dot{\psi} dV \geq 0 \end{aligned} \quad (\text{A.3})$$

where the governing Eqs. (2.1) and (2.16) has been considered for the free energy potential $\psi(\epsilon, d, \nabla d, C)$. Standard arguments then yield the following thermodynamically consistent constitutive relations

$$\begin{cases} \boldsymbol{\sigma} = \frac{\partial \psi}{\partial \boldsymbol{\epsilon}} \\ \mathbf{q} = \frac{\partial \psi}{\partial \nabla d} \\ Q = -\frac{\partial \psi}{\partial d} \\ \mu = \frac{\partial \psi}{\partial C} \end{cases} \quad (\text{A.4})$$

Moreover, the associated energy dissipation inequality reads

$$\dot{\mathcal{D}} = - \int_{\Omega} \mathbf{J} \cdot \nabla \mu \, dV \geq 0 \quad (\text{A.5})$$

As can be seen, the following Fick law

$$\mathbf{J} = - \frac{DC}{RT} \nabla \mu \quad (\text{A.6})$$

automatically fulfills the energy dissipation inequality (A.5).

Specifically, let us consider the following free energy potential [102]

$$\begin{aligned} \psi = & \underbrace{\omega(d) \frac{1}{2} \epsilon : \mathbb{E}_0 : \epsilon}_{\text{bulk strain energy}} + \underbrace{G_f \frac{1}{c_a} \left(\frac{1}{b} \alpha(d) + b |\nabla d|^2 \right)}_{\text{crack surface energy}} \\ & + \underbrace{\left[\mu_0 C + RT (C \ln C - C) \right]}_{\text{chemical free energy}} - \underbrace{\omega(d) K_0 V_H (C - C_0) \text{tr} \epsilon}_{\text{Coupled chemo-mechanical energy}} \end{aligned} \quad (\text{A.7})$$

where C_0 and μ_0 are the reference hydrogen concentration and chemical potential, respectively; $K_0 = \frac{\bar{\epsilon}_0}{3(1-2\nu_0)}$ is the bulk modulus. It then follows that

$$\sigma = \omega(d) \mathbb{E}_0 : \epsilon - \omega(d) K_0 V_H (C - C_0) \mathbf{1} \quad (\text{A.8a})$$

$$Q = -\omega'(d) \bar{Y} - \frac{G_f}{c_a b} \alpha'(d) + \omega'(d) K_0 V_H (C - C_0) \text{tr} \epsilon \quad (\text{A.8b})$$

$$\mathbf{q} = \frac{2b}{c_a} G_f \nabla d \quad (\text{A.8c})$$

$$\mu = \mu_0 + RT \ln C - V_H \sigma_H \quad (\text{A.8d})$$

$$\mathbf{J} = -D \nabla C + \frac{DV_H}{RT} C \nabla \sigma_H \quad (\text{A.8e})$$

where $\sigma_H = \omega(d) K_0 \text{tr} \epsilon = \text{tr} \sigma / 3$ is the hydrostatic stress. Regarding hydrogen embrittlement phenomena, the second term in Eq. (A.8a) and the third one in Eq. (A.8b) related to the chemo-mechanical coupling have negligible effects and can be omitted to recover the constitutive relations given in Eqs. (2.1c), (2.3) and (2.17), respectively.

References

- [1] T. Rabczuk, Computational methods for fracture in brittle and quasi-brittle solids: State-of-the-art review and future perspectives, ISRN Appl. Math. 2013 (2013) <http://dx.doi.org/10.1155/2013/849231>.
- [2] G.A. Francfort, J.-J. Marigo, Revisiting brittle fracture as an energy minimization problem, J. Mech. Phys. Solids 46 (8) (1998) 1319–1342.
- [3] B. Bourdin, G.A. Francfort, J.-J. Marigo, Numerical experiments in revisited brittle fracture, J. Mech. Phys. Solids 48 (4) (2000) 797–826.
- [4] C. Miehe, F. Welschinger, M. Hofacker, Thermodynamically consistent phase-field models of fracture: Variational principles and multi-field FE implementations, Internat. J. Numer. Methods Engrg. 83 (2010) 1273–1311.
- [5] B. Bourdin, G.A. Francfort, J.-J. Marigo, The variational approach to fracture, J. Elasticity 91 (1–3) (2008) 5–148.
- [6] M. Ambati, T. Gerasimov, L. De Lorenzis, A review on phase-field models of brittle fracture and a new fast hybrid formulation, Comput. Mech. 55 (2) (2015) 383–405.
- [7] J.Y. Wu, V.P. Nguyen, C.T. Nguyen, D. Sutula, S. Sinaie, S. Bordas, Phase field modeling of fracture, Adv. Appl. Mech. Fract. Mech. Recent Dev. Trends Vol. 53 (2019) in press.
- [8] M.J. Borden, T.J. Hughes, C.M. Landis, A. Anvari, I.J. Lee, A phase-field formulation for fracture in ductile materials: Finite deformation balance law derivation, plastic degradation, and stress triaxiality effects, Comput. Methods Appl. Mech. Engrg. 312 (2016) 130–166.
- [9] C. Kuhn, T. Noll, R. Müller, On phase field modeling of ductile fracture, GAMM-Mitt. 39 (1) (2016) 35–54.
- [10] C. Miehe, F. Welschinger, M. Hofacker, Thermodynamically consistent phase-field models of fracture: Variational principles and multi-field FE implementations, Internat. J. Numer. Methods Engrg. 83 (10) (2010) 1273–1311.
- [11] K. Pham, H. Amor, J.-J. Marigo, C. Maurini, Gradient damage models and their use to approximate brittle fracture, Int. J. Damage Mech. 20 (4) (2011) 618–652.
- [12] M. Borden, T. Hughes, C. Landis, C. Verhoosel, A higher-order phase-field model for brittle fracture: formulation and analysis within the isogeometric analysis framework, Comput. Methods Appl. Mech. Engrg. 273 (2014) 100–118.
- [13] A.A. Griffith, The phenomena of rupture and flow in solids, Philos. Trans. Royal Soc. Londres 221 (1920) 163–198.
- [14] A. Mesgarnejad, B. Bourdin, M. Khonsari, Validation simulations for the variational approach to fracture, Comput. Methods Appl. Mech. Engrg. 290 (2015) 420–437.
- [15] E. Tanné, T. Li, B. Bourdin, J.-J. Marigo, C. Maurini, Crack nucleation in variational phase-field models of brittle fracture, J. Mech. Phys. Solids 110 (2018) 80–99.
- [16] A. Kumar, B. Bourdin, G.A. Francfort, O. Lopez-Pamies, Revisiting nucleation in the phase-field approach to brittle fracture, J. Mech. Phys. Solids 142 (2020) 104027.
- [17] M. Strobl, T. Seelig, Phase field modeling of hertzian indentation fracture, J. Mech. Phys. Solids 143 (2020) 104026.
- [18] T.K. Mandal, V.P. Nguyen, J.Y. Wu, Length scale and mesh bias sensitivity of phase-field models for brittle and cohesive fracture, Eng. Fract. Mech. 217 (2019) 106532.
- [19] J.Y. Wu, A unified phase-field theory for the mechanics of damage and quasi-brittle failure in solids, J. Mech. Phys. Solids 103 (2017) 72–99.
- [20] J.Y. Wu, A geometrically regularized gradient-damage model with energetic equivalence, Comput. Methods Appl. Mech. Engrg. 328 (2018a) 612–637.
- [21] J.Y. Wu, V.P. Nguyen, A length scale insensitive phase-field damage model for brittle fracture, J. Mech. Phys. Solids 119 (2018) 20–42.
- [22] G.I. Barenblatt, The formation of equilibrium cracks during brittle fracture. General ideas and hypotheses. Axially-symmetric cracks, J. Appl. Math. Mech. 23 (1959) 622–636.
- [23] D.C. Feng, J.Y. Wu, Phase-field regularized cohesive zone model (CZM) and size effect of concrete, Eng. Fract. Mech. 197 (2018) 66–79.
- [24] J.Y. Wu, J.F. Qiu, V.P. Nguyen, T.K. Mandal, L.J. Zhuang, Computational modeling of localized failure in solids: XFEM vs PF-CZM, Comput. Methods Appl. Mech. Engrg. 345 (2019) 618–643.
- [25] V.P. Nguyen, J.-Y. Wu, Modeling dynamic fracture of solids with a phase-field regularized cohesive zone model, Comput. Methods Appl. Mech. Engrg. 340 (2018) 1000–1022.
- [26] A. Marbœuf, L. Bennani, M. Budinger, V. Pommier-Budinger, Electromechanical resonant ice protection systems: numerical investigation through a phase-field mixed adhesive/brittle fracture model, Eng. Fract. Mech. 230 (2020) 106926.
- [27] P.J. Loew, B. Peters, L.A.A. Beex, Fatigue phase-field damage modeling of rubber using viscous dissipation: Crack nucleation and propagation, Mech. Mater. 142 (2020) 103282.
- [28] P.J. Loew, L.H. Poh, B. Peters, L.A.A. Beex, Accelerating fatigue simulations of a phase-field damage model for rubber, Comput. Methods Appl. Mech. Engrg. 370 (2020) 113247.
- [29] B. Bourdin, J.-J. Marigo, C. Maurini, P. Sicsic, Morphogenesis and propagation of complex cracks induced by thermal shocks, Phys. Rev. Lett. 112 (1) (2014) 014301.
- [30] C. Miehe, L.-M. Schaezel, H. Ulmer, Phase field modeling of fracture in multi-physics problems. Part I. balance of crack surface and failure criteria for brittle crack propagation in thermo-elastic solids, Comput. Methods Appl. Mech. Engrg. 294 (2015) 449–485.
- [31] C. Miehe, F. Welschinger, M. Hofacker, A phase field model of electromechanical fracture, J. Mech. Phys. Solids 58 (10) (2010) 1716–1740.
- [32] Z.A. Wilson, M.J. Borden, C.M. Landis, A phase-field model for fracture in piezoelectric ceramics, Int. J. Fract. 183 (2) (2013) 135–153.
- [33] A. Abdollahi, I. Arias, Phase-field modeling of crack propagation in piezoelectric and ferroelectric materials with different electromechanical crack conditions, J. Mech. Phys. Solids 60 (12) (2012) 2100–2126.
- [34] T.-T. Nguyen, D. Waldmann, T.Q. Bui, Computational chemo-thermo-mechanical coupling phase-field model for complex fracture induced by early-age shrinkage and hydration heat in cement-based materials, Comput. Methods Appl. Mech. Engrg. 348 (2019) 1–28.
- [35] T.-T. Nguyen, D. Waldmann, T.Q. Bui, Phase field simulation of early-age fracture in cement-based materials, Int. J. Solids Struct. 191 (2020) 157–172.
- [36] E.M.-P. neda, A. Golahmar, C.F. Niordson, A phase field formulation for hydrogen assisted cracking, Comput. Methods Appl. Mech. Engrg. 342 (2018) 742–761.
- [37] P.K. Kristensen, C.F. Niordson, E. Martínez-Pañeda, Applications of phase field fracture in modelling hydrogen assisted failures, Theor. Appl. Fract. Mech. 110 (2020) 102837.
- [38] T. Wu, L. De Lorenzis, A phase-field approach to fracture coupled with diffusion, Comput. Methods Appl. Mech. Engrg. 312 (2016) 196–223.
- [39] L. Schuler, A.G. Ilgen, P. Newell, Chemo-mechanical phase-field modeling of dissolution-assisted fracture, Comput. Methods Appl. Mech. Engrg. 362 (2020) 112838.
- [40] J.-Y. Wu, T.K. Mandal, V.P. Nguyen, A phase-field regularized cohesive zone model for hydrogen assisted cracking, Comput. Methods Appl. Mech. Engrg. 358 (2020) 112614.
- [41] T.K. Mandal, V.P. Nguyen, J.Y. Wu, Comparative study of phase-field damage models for hydrogen assisted cracking, Theor. Appl. Fract. Mech. 111 (2021) 102840.
- [42] T.K. Mandal, V.P. Nguyen, J.Y. Wu, C. Nguyen-Thanh, A. de Vaucorbeil, Fracture of thermo-elastic solids: Phase-field modeling and new results with an efficient monolithic solver, Comput. Methods Appl. Mech. Engrg. 376 (2021) 113648.

- [43] C. Kuhn, A. Schlüter, R. Müller, On degradation functions in phase field fracture models, *Comput. Mater. Sci.* 108 (2015) 374–384.
- [44] T. Li, J.-J. Marigo, D. Guilbaud, S. Potapov, Gradient damage modeling of brittle fracture in an explicit dynamics context, *Internat. J. Numer. Methods Engrg.* 108 (11) (2016) 1381–1405.
- [45] M. Klinsmann, D. Rosato, M. Kamlah, R.M. McMeeking, An assessment of the phase field formulation for crack growth, *Comput. Methods Appl. Mech. Engrg.* 294 (2015) 313–330.
- [46] T. Heister, M.F. Wheeler, T. Wick, A primal-dual active set method and predictor-corrector mesh adaptivity for computing fracture propagation using a phase-field approach, *Comput. Methods Appl. Mech. Engrg.* 290 (2015) 466–495.
- [47] M.F. Wheeler, T. Wick, S. Lee, Ipacs: Integrated phase-field advanced crack propagation simulator. An adaptive, parallel, physics-based-discretization phase-field framework for fracture propagation in porous media, *Comput. Methods Appl. Mech. Engrg.* 367 (2020) 113124.
- [48] P. Chakraborty, Y. Zhang, M.R. Tonks, Multi-scale modeling of microstructure dependent intergranular brittle fracture using a quantitative phase-field based method, *Comput. Mater. Sci.* 113 (2016) 38–52.
- [49] S. Zhang, W. Jiang, M.R. Tonks, A new phase field fracture model for brittle materials that accounts for elastic anisotropy, *Comput. Methods Appl. Mech. Engrg.* 358 (2020) 112643.
- [50] T.T. Nguyen, J. Yvonnet, Q.-Z. Zhu, M. Bornert, C. Chateau, A phase field method to simulate crack nucleation and propagation in strongly heterogeneous materials from direct imaging of their microstructure, *Eng. Fract. Mech.* 139 (2015) 18–39.
- [51] T.-T. Nguyen, J. Réthoré, J. Yvonnet, M.-C. Baietto, Multi-phase-field modeling of anisotropic crack propagation for polycrystalline materials, *Comput. Mech.* 60 (2) (2017) 289–314.
- [52] C. Nguyen-Thanh, V.P. Nguyen, A. de Vaucorbeil, T.K. Mandal, J.-Y. Wu, Jive: an open source, research-oriented c++ library for solving partial differential equations, *Adv. Eng. Softw.* 150 (2020) 102925.
- [53] M.A. Msekh, J.M. Sargado, M. Jamshidian, P.M. Areias, T. Rabczuk, Abaqus implementation of phase-field model for brittle fracture, *Comput. Mater. Sci.* 96 (2015) 472–484.
- [54] G. Liu, Q. Li, M.A. Msekh, Z. Zuo, Abaqus implementation of monolithic and staggered schemes for quasi-static and dynamic fracture phase-field model, *Comput. Mater. Sci.* 121 (2016) 35–47.
- [55] G. Molnár, A. Gravouil, 2D and 3D abaqus implementation of a robust staggered phase-field solution for modeling brittle fracture, *Finite Elem. Anal. Des.* 130 (2017) 27–38.
- [56] G. Molnár, A. Gravouil, R. Seghir, J. Réthoré, An open-source abaqus implementation of the phase-field method to study the effect of plasticity on the instantaneous fracture toughness in dynamic crack propagation, *J. Mech. Phys. Solids* 365 (2020) 113004.
- [57] J.-Y. Wu, Y. Huang, Comprehensive implementations of phase-field damage models in abaqus, *Theor. Appl. Fract. Mech.* 106 (2020) 102440.
- [58] W. Zhang, A. Tabiei, D. French, A numerical implementation of the length-scale independent phase field method, *Acta Mech. Sinica* 37 (2021) 92–104.
- [59] Y. Hou, L. Wang, P. Yue, T. Pauli, W. Sun, Modeling mode I cracking failure in asphalt binder by using nonconserved phase-field model, *J. Mater. Civ. Eng.* 26 (4) (2014) 684–691.
- [60] S. Zhou, T. Rabczuk, X. Zhuang, Phase field modeling of quasi-static and dynamic crack propagation: COMSOL implementation and case studies, *Adv. Eng. Softw.* 122 (2018) 31–49.
- [61] S. Zhou, X. Zhuang, T. Rabczuk, Phase-field modeling of fluid-driven dynamic cracking in porous media, *Comput. Methods Appl. Mech. Engrg.* 350 (2019) 169–198.
- [62] C. Miehe, M. Hofacker, F. Welschinger, A phase field model for rate-independent crack propagation: Robust algorithmic implementation based on operator splits, *Comput. Methods Appl. Mech. Engrg.* 199 (45–48) (2010) 2765–2778.
- [63] J.-Y. Wu, V.P. Nguyen, H. Zhou, Y. Huang, A variationally consistent phase-field anisotropic damage model for fracture, *Comput. Methods Appl. Mech. Engrg.* 358 (2020) 112629.
- [64] J.-Y. Wu, Robust numerical implementation of non-standard phase-field damage models for failure in solids, *Comput. Methods Appl. Mech. Engrg.* 340 (2018) 767–797.
- [65] J.-Y. Wu, Y. Huang, H. Zhou, V.P. Nguyen, Three-dimensional phase-field modeling of mode I+ II/III failure in solids, *Comput. Methods Appl. Mech. Engrg.* 373 (2021) 113537.
- [66] H. Cornelissen, D. Hordijk, H. Reinhardt, Experimental determination of crack softening characteristics of normalweight and lightweight, *Heron* 31 (2) (1986) 45–46.
- [67] B. Bourdin, J.-J. Marigo, C. Maurini, P. Sicsic, Morphogenesis and propagation of complex cracks induced by thermal shocks, *Phys. Rev. Lett.* 112 (2014) 014301.
- [68] C. Miehe, L. Schänzel, H. Ulmer, Phase field modeling of fracture in multi-physics problems. Part I. balance of crack surface and failure criteria for brittle crack propagation in thermo-elastic solids, *Comput. Methods Appl. Mech. Engrg.* 294 (2015) 449–485.
- [69] D.A. Porter, K.E. Easterling, M. Sherif, *Phase Transformations in Metals and Alloys*, (Revised Reprint), CRC Press, 2009.
- [70] S. Serebrinsky, E. Carter, M. Ortiz, A quantum-mechanically informed continuum model of hydrogen embrittlement, *J. Mech. Phys. Solids* 52 (10) (2004) 2403–2430.
- [71] E. Hondros, M. Seah, The theory of grain boundary segregation in terms of surface adsorption analogues, *Metall. Trans. A* 8 (9) (1977) 1363–1371.
- [72] E. Martínez-Pañeda, A. Golahmar, C.F. Niordson, A phase field formulation for hydrogen assisted cracking, *Comput. Methods Appl. Mech. Engrg.* 342 (2018) 742–761.
- [73] F.-J. Ulm, O. Coussy, Modeling of thermochemomechanical couplings of concrete at early ages, *J. Eng. Mech.* 121 (7) (1995) 785–794.
- [74] M. Cervera, J. Oliver, T. Prato, Thermo-chemo-mechanical model for concrete. I: Hydration and aging, *J. Eng. Mech.* 125 (9) (1999) 1018–1027.
- [75] J.T. de Freitas, P. Cuong, R. Faria, M. Azenha, Modelling of cement hydration in concrete structures with hybrid finite elements, *Finite Elem. Anal. Des.* 77 (2013) 16–30.
- [76] T.-T. Nguyen, M. Weiler, D. Waldmann, Experimental and numerical analysis of early age behavior in non-reinforced concrete, *Constr. Build. Mater.* 210 (2019) 499–513.
- [77] J.-Y. Wu, W.-X. Chen, Computational modeling of shrinkage induced cracking in early-age concrete based on the unified phase-field theory, *Chin. J. Theor. Appl. Mech.* (2021).
- [78] V. Waller, Relationship Between Mix Design of Concrete, Generation of Heat During Hydration and Compressive Strength (Ph.D. thesis), Ph. D. thesis, École Nationale de Ponts et Chaussées, Paris, France, 1999.
- [79] G. De Schutter, L. Taerwe, Degree of hydration-based description of mechanical properties of early age concrete, *Mater. Struct.* 29 (6) (1996) 335–344.
- [80] G. De Schutter, Finite element simulation of thermal cracking in massive hardening concrete elements using degree of hydration based material laws, *Comput. Struct.* 80 (27–30) (2002) 2035–2042.
- [81] J.Y. Wu, W.X. Chen, A phase-field cohesive zone model (PF-CZM) for electromechanical fracture in piezoelectric solids: Analytical results and numerical simulations, *Comput. Methods Appl. Mech. Engrg.* (2021) under review.
- [82] W.F. Deeg, The Analysis of Dislocation, Crack, and Inclusion Problems in Piezoelectric Solids (Ph.D. thesis), Stanford University, 1981.
- [83] Y.E. Pak, Crack extension force in a piezoelectric material, *J. Appl. Mech.* (ISSN: 0021-8936) 57 (3) (1990) 647–653.
- [84] Z. Suo, C.-M. Kuo, D. Barnett, J. Willis, Fracture mechanics for piezoelectric ceramics, *J. Mech. Phys. Solids* 40 (4) (1992) 739–765.
- [85] H. Gao, T.-Y. Zhang, P. Tong, Local and global energy release rates for an electrically yielded crack in a piezoelectric ceramic, *J. Mech. Phys. Solids* 45 (4) (1997) 491–510.
- [86] J.-Y. Wu, Y. Huang, V.P. Nguyen, On the BFGS monolithic algorithm for the unified phase field damage theory, *Comput. Methods Appl. Mech. Engrg.* 360 (2020) 112704.
- [87] H. Amor, J.-J. Marigo, C. Maurini, Regularized formulation of the variational brittle fracture with unilateral contact: Numerical experiments, *J. Mech. Phys. Solids* 57 (8) (2009) 1209–1229.
- [88] T. Gerasimov, L. De Lorenzis, A line search assisted monolithic approach for phase-field computing of brittle fracture, *Comput. Methods Appl. Mech. Engrg.* 312 (2016) 276–303.
- [89] T. Wick, Modified Newton methods for solving fully monolithic phase-field quasi-static brittle fracture propagation, *Comput. Methods Appl. Mech. Engrg.* 325 (2017) 577–611.
- [90] R. de Borst, Computation of post-bifurcation and post-failure behavior of strain-softening solids, *Comput. Struct.* 25 (1987) 211–224.
- [91] P. Wriggers, J. Simó, A general procedure for the direct computation of turning and bifurcation points, *Internat. J. Numer. Methods Engrg.* 30 (1990) 155–176.
- [92] H. Cornelissen, D. Hordijk, H. Reinhardt, Experimental determination of crack softening characteristics of normalweight and lightweight concrete, *Heron* 31 (2) (1986) 45–56.
- [93] K. Pham, K. Ravi-Chandar, C. Landis, Experimental validation of a phase-field model for fracture, *Int. J. Fract.* 205 (1) (2017) 83–101.
- [94] M. Arrea, Mixed-mode crack propagation in mortar and concrete, *Dept. Struct. Eng. Rep.* (1981) 13–81.
- [95] C. Linder, F. Armero, Finite elements with embedded strong discontinuities for the modeling of failure in solids, *Internat. J. Numer. Methods Engrg.* 72 (12) (2007) 1391–1433.
- [96] C. Jiang, X. Wu, J. Li, F. Song, Y. Shao, X. Xu, P. Yan, A study of the mechanism of formation and numerical simulations of crack patterns in ceramics subjected to thermal shock, *Acta Mater.* 60 (11) (2012) 4540–4550.
- [97] S. Tang, H. Zhang, C. Tang, H. Liu, Numerical model for the cracking behavior of heterogeneous brittle solids subjected to thermal shock, *Int. J. Solids Struct.* 80 (2016) 520–531.
- [98] D. Chu, X. Li, Z. Liu, Study the dynamic crack path in brittle material under thermal shock loading by phase field modeling, *Int. J. Fract.* 208 (1) (2017) 115–130.
- [99] Y. Wang, X. Zhou, M. Kou, An improved coupled thermo-mechanic bond-based peridynamic model for cracking behaviors in brittle solids subjected to thermal shocks, *Eur. J. Mech. A Solids* 73 (2019) 282–305.

- [100] J. Li, F. Song, C. Jiang, Direct numerical simulations on crack formation in ceramic materials under thermal shock by using a non-local fracture model, *J. Eur. Ceram. Soc.* 33 (13–14) (2013) 2677–2687.
- [101] M. Wang, E. Akiyama, K. Tsuzaki, Effect of hydrogen and stress concentration on the notch tensile strength of AISI 4135 steel, *Mater. Sci. Eng. A* 398 (1–2) (2005) 37–46.
- [102] E.M.-P. neda, A. Golahmar, C.F. Niordson, A phase field formulation for hydrogen assisted cracking, *Comput. Methods Appl. Mech. Engrg.* 342 (2018) 742–761.
- [103] A.B. Hossain, J. Weiss, Assessing residual stress development and stress relaxation in restrained concrete ring specimens, *Cem. Concr. Compos.* 26 (5) (2004) 531–540.
- [104] M. Briffaut, F. Benboudjema, J.M. Torrenti, G. Nahas, Numerical analysis of the thermal active restrained shrinkage ring test to study the early age behavior of massive concrete structures, *Eng. Struct.* 33 (4) (2011) 1390–1401.
- [105] S. Park, C.-T. Sun, Fracture criteria for piezoelectric ceramics, *J. Am. Ceram. Soc.* 78 (6) (1995) 1475–1480.